Development of a physically based dust emission module within the Weather Research and Forecasting (WRF) model: Assessment of dust emission parameterizations and input parameters for source regions in Central and East Asia

Kremena Darmenova, Irina N Sokolik, Yaping Shao, Beatrice Marticorena, Gilles Bergametti

JOURNAL OF GEOPHYSICAL RESEARCH, VOL. 114, D14201, doi:10.1029/2008JD011236, 2009

Development of a physically based dust emission module within the Weather Research and Forecasting (WRF) model: Assessment of dust emission parameterizations and input parameters for source regions in Central and East Asia

Kremena Darmenova,[1] Irina N. Sokolik,[1] Yaping Shao,[2] Beatrice Marticorena,[3] and Gilles Bergametti[3]

Received 2 October 2008; revised 19 February 2009; accepted 30 April 2009; published 16 July 2009.

[1] Significant problems with modeling dust emission are highlighted. Not only do dust emission schemes rely on various assumptions, but also their implementation within a regional or global model presents challenges. This paper provides an in-depth comparative analysis of two different physically based schemes that were originally developed by Marticorena and Bergametti (1995) and Shao et al. (1996) with some recent improvements. Both schemes were implemented in a dust module (DuMo) and coupled with the Weather Research and Forecasting (WRF) model. Here we examine the physical parameterizations employed by these schemes, identify the key input parameters, and establish linkages between them by developing a new data set for dust sources in Central and East Asia. The relative importance of the input parameters is assessed through partial derivatives. The major issues involved in implementing the physically based schemes within a regional model are also discussed. Consistent implementation of two state-of-the-art dust schemes within the same regional model enables us to bracket inherent uncertainties in simulated dust emission. The results of a case study based on WRF–DuMo simulations are presented to demonstrate associated biases in the magnitude and spatial patterns of emitted dust vertical fluxes. Also, recommendations on the selection of input parameters, including land and meteorological variables, to achieve an improved modeling of dust emission in Central and East Asia are provided.

Citation: Darmenova, K., I. N. Sokolik, Y. Shao, B. Marticorena, and G. Bergametti (2009), Development of a physically based dust emission module within the Weather Research and Forecasting (WRF) model: Assessment of dust emission parameterizations and input parameters for source regions in Central and East Asia, *J. Geophys. Res.*, *114*, D14201, doi:10.1029/2008JD011236.

1. Introduction

[2] The potential of mineral aerosols (dust) to affect the Earth system has been recognized for some time [*Duce*, 1995; *Tegen and Fung*, 1994; *Sokolik et al.*, 2001]. Dust particles affect the radiative transfer in the solar and thermal infrared wavelengths and hence can alter the energy balance, thermodynamics, dynamics, and chemistry of the atmosphere [*Sokolik*, 2003; *Intergovernmental Panel on Climate Change* (*IPCC*), 2007]. The radiative forcing of dust particles is further augmented by their interactions with clouds, other atmospheric aerosols, or gases, leading to diverse impacts upon Earth's energy balance, as well as on biogeochemical and hydrological cycles. Recognizing the important role that dust plays in the natural climate system, and most likely in climate change, all general circulation models (GCMs) used in the *IPCC* [2007] climate change assessment included mineral dust among other major types of atmospheric aerosols. Furthermore, many regional (mesoscale) models, as well as some numerical weather prediction models now include dust [e.g., *Liu et al.*, 2003; *Sun et al.*, 2006]. However, the results vary strongly among modeling studies because of various challenges associated with representing mineral aerosols in GCMs and regional models [*Zender et al.*, 2003; *Uno et al.*, 2006]. A recent model intercomparison [e.g., *Uno et al.*, 2006; *Todd et al.*, 2008] demonstrates that dust emission remains a key source of significant errors, pointing to an urgent need to improve dust emission modeling.

[3] The dust emission, aeolian (wind) erosion that results in the production of mineral aerosols from soil grains, involves complex, nonlinear processes that are governed by the meteorology as well as by the state and properties of land surfaces. Although many aspects of wind erosion are reasonably well understood, what is known comes largely from microscale (local) experiments and theoretical studies.

[1] School of Earth and Atmospheric Sciences, Georgia Institute of Technology, Atlanta, Georgia, USA.
[2] Institute of Geophysics and Meteorology, University of Cologne, Cologne, Germany.
[3] Laboratoire Interuniversitaire des Systèmes Atmosphériques, Universités Paris VII-XII, Creteil, France.

0148-0227/09/2008JD011236$09.00

Given the difficulty of making representative measurements of emitted dust fluxes and all required land and atmospheric properties, development of physically based parameterizations of dust production remains a challenging problem. Even if high-quality local measurements of emitted dust fluxes could be made, the inhomogeneity and temporal variability of land surfaces and meteorological fields make such measurements unrepresentative of the area- and time-average fluxes at the scales needed for input into regional and global models. Thus, not only do dust emission schemes rely on various assumptions, but also their implementation within a regional or global model presents challenges. The latter was clearly demonstrated by *Todd et al.* [2008], who showed significant biases between different regional models that implement the same dust emission scheme.

[4] In this study, we present an in-depth analysis of two physically based dust emission schemes that were implemented within the Weather Research and Forecasting (WRF) model. One dust scheme was originally developed by *Marticorena and Bergametti* [1995], while another was developed by *Shao et al.* [1996] with some recent improvements (herein after denoted by MB and Shao, respectively). These schemes offer a number of advantages compared to the so-called simple dust emission schemes, which are being widely used in dust modeling [e.g., *Tegen and Fung*, 1994; *Uno et al.*, 2001; *Liu et al.*, 2003]. Simple schemes parameterize the vertical flux of emitted mineral aerosols in terms of the third (or fourth) power of the surface wind speed (or the friction velocity), while several parameters (such as an erodible fraction and a mass normalization constant) are assigned arbitrarily for predefined dust sources [*Darmenova and Sokolik*, 2007]. In particular, the threshold friction velocity, which is a key parameter governing the initiation of dust entrainment, is fixed uniformly, despite the fact that it varies in space and time, depending on meteorological and land surface characteristics. In contrast, the MB and Shao dust schemes offer physically based parameterizations of related processes that explicitly take into account the surface characteristics when calculating the threshold friction velocity, and the size-resolved horizontal (saltation) and vertical dust fluxes. Although there are some similarities between these two dust schemes, they do evoke different approaches to parameterization of related processes and require different input data. Thus implementation of these schemes into a regional model necessitates a step-by-step intercomparison of the scientific foundation of parameterizations, as well as the development of a database to provide input parameters required by both schemes in a consistent fashion. We are not aware of any previous study that has comprehensively addressed these issues, and this is one of the goals of the present paper.

[5] A dust emission scheme requires both meteorological and land surface characteristics at temporal and spatial scales pertinent to dust emission processes (called aeolian scales). Some data and parameters are readily available within a regional model framework, since it is designed to simulate the meteorological fields as well as land surface characteristics involved in land–atmosphere interaction processes, such as hydrological processes, vegetation dynamics, and energy balance. In particular, each mesoscale model includes a land module. Regardless of its level of complexity, none of the developed land surface models has been designed with the purpose to model dust emission. Due to specifics of dust emission processes, properties of the uppermost (1–2 cm thick) soil layer are needed to provide input to the dust scheme (e.g., soil moisture); however, this fine scale is not resolved by the land module within the regional or global model. Furthermore, land models do not provide several key input parameters needed in the dust scheme. For instance, both the MB and Shao schemes require an "undisturbed" soil particle size distribution (i.e., a dry-sieved size distribution of soil grains in the uppermost land surface layer), whereas the land models commonly use the classical sedimentological textural triangle. On the basis of experimental data from several desert sites in China, *Laurent et al.* [2006] pointed out that there is no direct relationship between the soil texture and the "undisturbed" soil particles size distribution. Addressing these issues requires the development of a new data set to provide land surface properties specific to dust mobilization processes that need to be incorporated into the regional model along with the dust emission scheme. To this end, the focus of this paper is on the vast dry lands of Central and East Asia that are prodigious sources of wind-blown mineral aerosols.

[6] The quantification of dust emission in the Asian region is hampered by its complex geomorphological and topographical features. In Central Asia, dust sources comprise a variety of sandy deserts of ancient alluvial plains, pebble/gravel/stony deserts, loamy deserts, loess deserts of piedmont planes, clayey takyrs, and solonchaks in saline depressions and along the sea coasts [*Lioubimtseva et al.*, 2005]. The East Asian dust sources also show notable heterogeneity, including sandy deserts, various pebble and stony deserts, sandy lands, and degraded agricultural lands [*Chao*, 1984]. A number of studies have been carried out to simulate the dust emission in East Asia using regional models [e.g., *Shao et al.*, 2002; *Gong et al.*, 2003; *Sun et al.*, 2006], while much less attention has been paid to Central Asia. However, *Uno et al.* [2006] revealed significant discrepancies in the simulated dust fields in East Asia among six regional and two global dust models. The majority of compared models use simple dust emission schemes. Thus improving dust emission parameterizations along with taking into account the region-specific properties of dust sources would be critical to make dust emission modeling more realistic at both regional and global scales.

[7] An outstanding question, which is rarely being addressed, is how to quantify errors of modeled dust fluxes. Available observations do not provide direct constraints of vertical fluxes of emitted dust. In turn, assessing the errors within the regional or global model is a formidable undertaking. As a result, the majority of past studies do not report errors associated with simulated dust emission at all. Having two differing physical schemes implemented within the same regional model provides a means to bracket the uncertainty of modeled vertical dust fluxes, thus contributing toward better assessment of errors. Here we present the case study of simulations performed with WRF–DuMo, which includes both MB and Shao schemes, for Asian dust sources. The WRF-DuMo modeling system was driven by the NCEP reanalysis data to reproduce the meteorological fields for the April 1998 time period, which is discussed here.

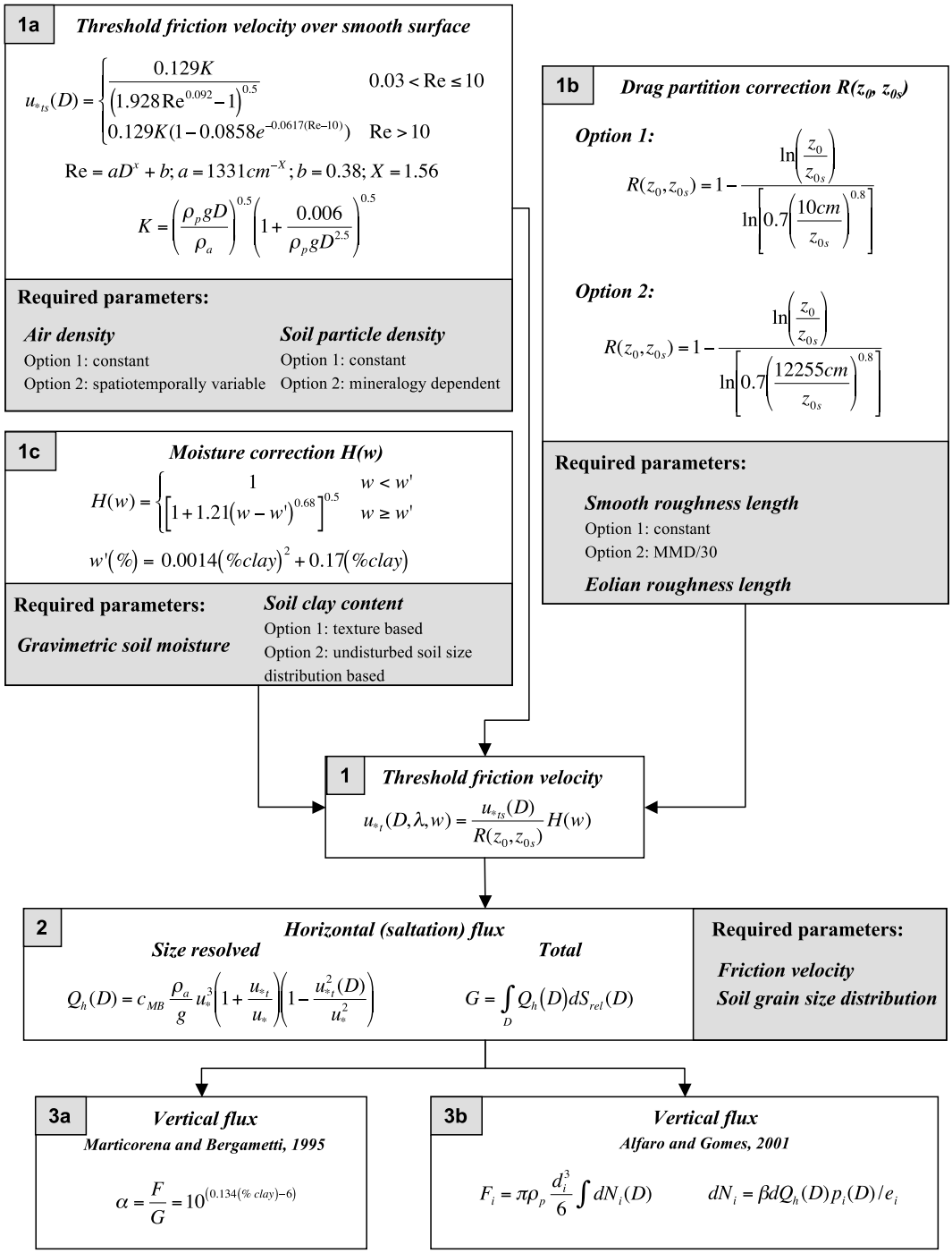

Figure 1. Schematic diagram of parameterization options and required input parameters in the MB dust emission scheme.

[8] The goals of this paper are to (1) examine the similarities and differences between the MB and Shao physical parameterizations of the dust emission process, addressing their range of applicability and inherent limitations; (2) identify required input parameters and perform an in-depth intercomparison between the two schemes considering the range of these parameters that are representative of Central and East Asia; and (3) explore the availability and relative importance of input parameters within the framework of a regional dust modeling system. The paper is organized as follows: section 2 examines the physical components of the MB and Shao dust emission schemes. Sections 3–5 discuss the step-by-step testing, and sensitivity analysis of these schemes, addressing the issues related to threshold friction velocity, and horizontal and vertical dust fluxes. Section 6 presents the results of dust emission simulations for Central and East Asia, focusing on the spatial patterns of vertical dust fluxes calculated with the MB and

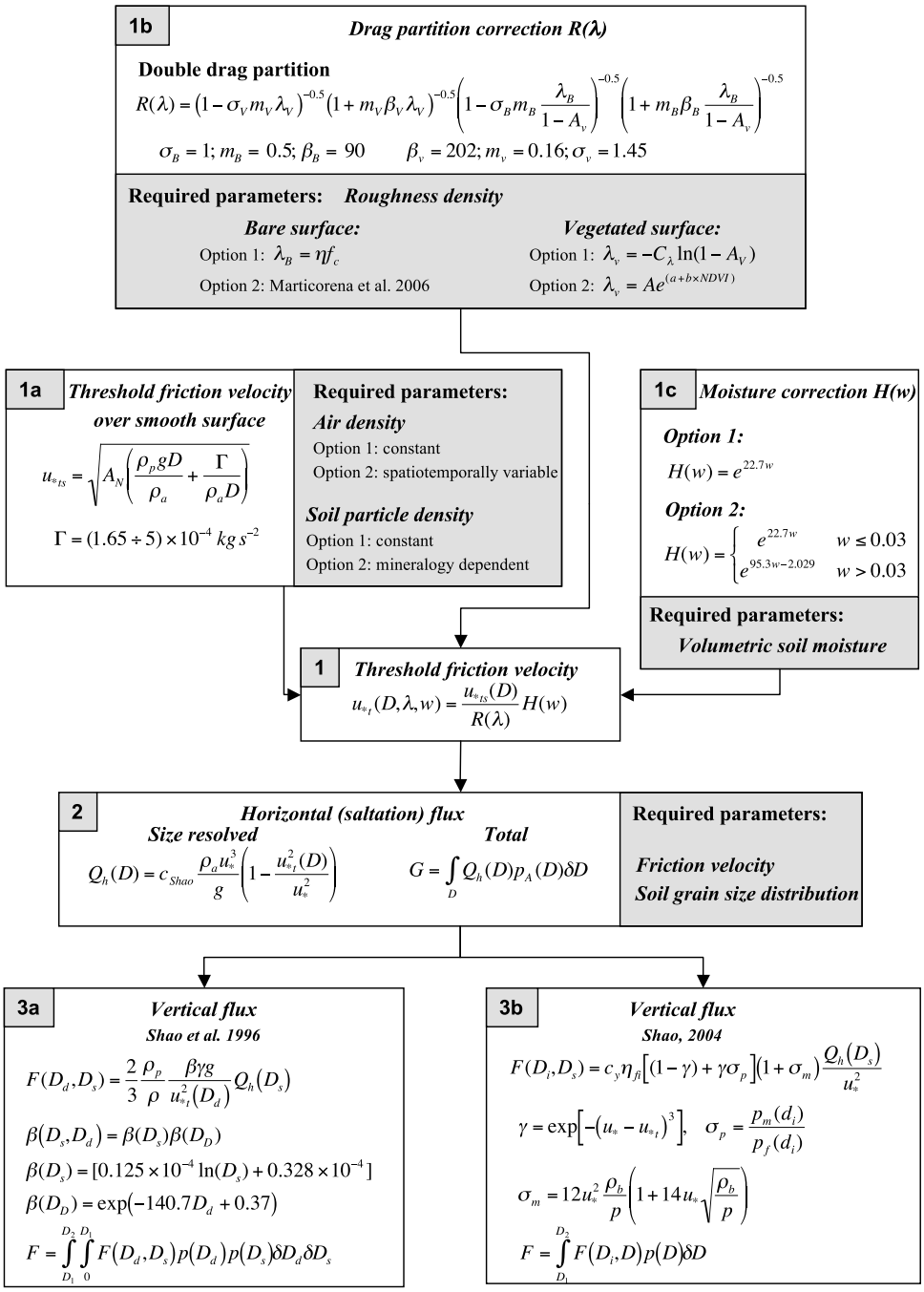

Figure 2. Schematic diagram of parameterization options and required input parameters in the Shao dust emission scheme.

Shao schemes. Section 7 summarizes the findings of this paper and provides recommendations.

2. Physical Parameterization of Dust Emission

[9] To adequately model the emission processes, a dust production scheme must accurately predict (1) the threshold friction velocity that is required to initiate soil particle motion under particular meteorological and land surface conditions; (2) the horizontal (or saltation) flux defined as the vertical integral of the stream-wise soil flux density (in units of g cm^{-1} s^{-1}); and (3) the vertical dust flux, which is defined as the mass of emitted dust from unit area per unit time (in g cm^{-2} s^{-1}). Figures 1 and 2 show these three major components in the MB and Shao dust emission schemes, schematically represented in modules 1, 2, and 3, respectively.

[10] Here we consider two parameterizations to compute the vertical dust flux F that were developed by *Alfaro and Gomes* [2001] and *Shao et al.* [1996] and are being used in the MB and Shao dust emission schemes, respectively. The *Alfaro and Gomes* [2001] model assumes that the kinetic energy of the saltating soil grains is used entirely for separating dust particles, whereas the Shao model relates

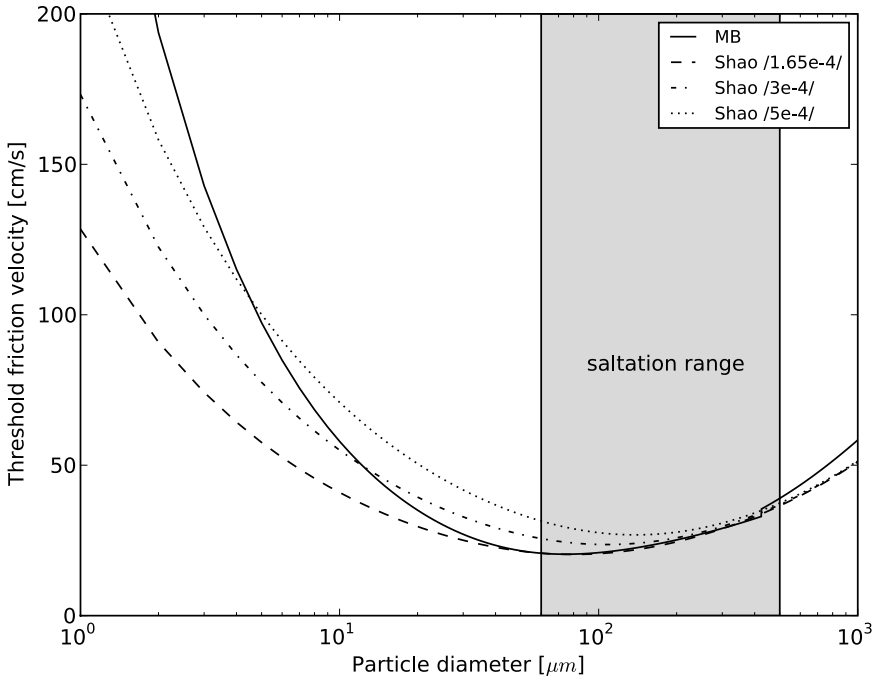

Figure 3. Threshold friction velocity over a smooth surface calculated with MB and Shao dust emission schemes.

the binding energy of dust-sized particles to their threshold friction velocity (see module 3 in Figures 1 and 2).

[11] Adequate quantification of the saltation flux for specific meteorological and land surface conditions is a necessary, key step in a dust production scheme. The saltation flux Q is commonly expressed as a function of the friction velocity, u_*, and the threshold friction velocity, u_{*t} [*Owen*, 1964] (see module 2 in Figures 1 and 2). The threshold friction velocity is defined as the minimum friction velocity required to initiate the motion of soil grains (see module 1 in Figures 1 and 2), and it depends on the soil type, roughness elements (such as vegetation, pebbles, cobbles, or stones), surface crusting, and soil moisture. These factors are taken into account by introducing the correction functions that are applied to the threshold friction velocity of an ideal "smooth" and dry surface (see module 1a in Figures 1 and 2). The two main factors that control the threshold friction velocity are surface roughness elements and soil moisture (see modules 1b and 1c in Figures 1 and 2). Both factors result in suppression of dust emission: the former by absorbing the momentum transferred from the wind shear to the surface and the latter by enhancing the interparticle cohesive forces.

[12] In sections 3–5 we examine the required parameters (shown in the shaded modules in Figures 1 and 2), the sensitivity of the dust production schemes to these parameters, and their availability within the framework of the regional dust modeling system.

3. Threshold Friction Velocity

[13] The threshold friction velocity for an arbitrary surface is expressed as follows:

$$u_{*t}(D,\lambda,w) = \frac{u_{*ts}(D)}{R} H, \qquad (1)$$

where $u_{*ts}(D)$ is the threshold friction velocity over the smooth surface and D is the diameter of soil particles. Here R is the drag partition correction that accounts for the presence of nonerodible elements (rocks, pebble, vegetation, etc.) in natural land surfaces. The roughness elements decrease the dust emission potential by sheltering the surface from aeolian erosion and by consuming part of the wind momentum otherwise transferred to the erodible surface. The moisture correction, H, is introduced to account for the suppression of soil erosion in wet soils due to increased cohesion.

3.1. Threshold Friction Velocity Over a Smooth Surface

[14] The threshold friction velocity over a smooth surface depends on the forces acting on a soil particle located over a bed of similar, equally sized soil particles. The MB scheme uses a parameterization developed by *Iversen and White* [1982] and *Greeley and Iversen* [1985]. It is difficult to apply this parameterization directly because of the dependence of the Reynolds number on soil particle diameter. To overcome this problem, *Marticorena and Bergametti* [1995] parameterized the Reynolds number for representative arid conditions as a power function of particle diameter (see module 1a in Figure 1). In turn, *Shao and Lu* [2000] proposed an expression that explicitly treats the cohesive force in the original equations of *Greeley and Iversen* [1985]. Shao and Lu assumed that the cohesive force is linearly proportional to soil particle size. An equation for the threshold friction velocity was derived by fitting to the data reported by *Iversen and White* [1982].

[15] Figure 3 compares the threshold friction velocity over a smooth surface calculated with the MB and Shao schemes. The Shao and Lu equation is plotted for three different values of Γ, a parameter accounting for the

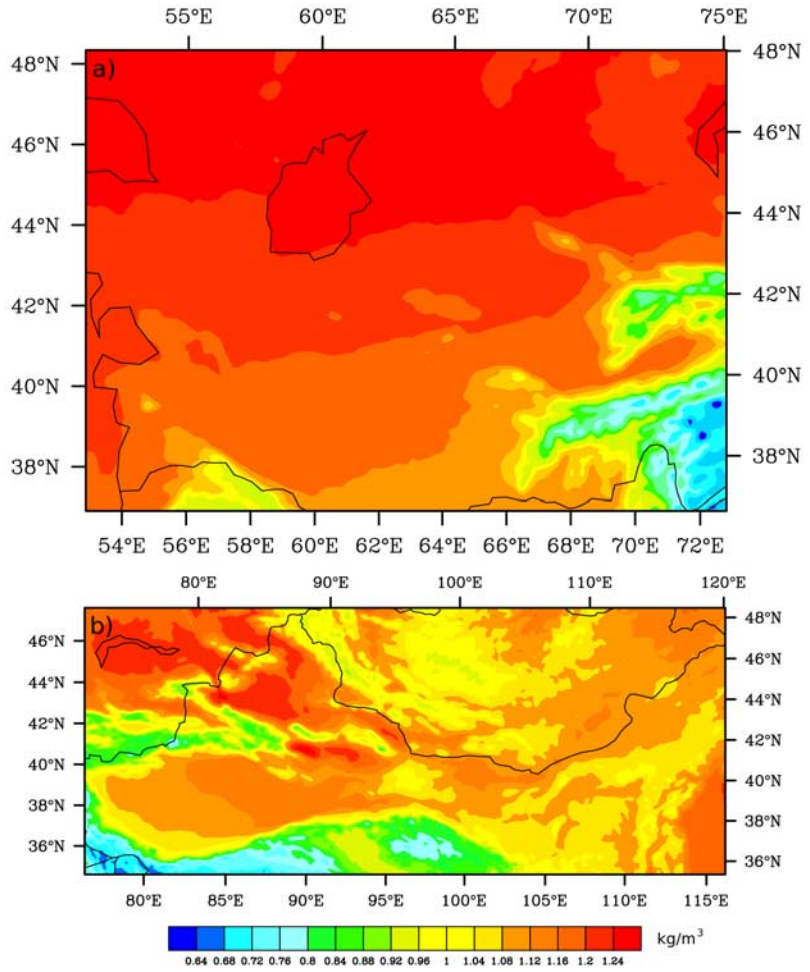

Figure 4. Average air density during the spring 2001 dust storm for (a) Central Asia and (b) East Asia.

magnitude of the cohesive force (see module 1a in Figure 2): 1.65×10^{-4}, 3×10^{-4}, and 5×10^{-4} kg/s^2. Both parameterizations show similar behavior of u_{*t} as a function of soil particle diameter. The lowest values of u_{*ts} in both schemes correspond to soil particle diameters from 65 to 200 μm, which reside in a typical saltation range of 60–500 μm (see shaded area of Figure 3). For smaller particles, u_{*ts} increases rapidly as a result of interparticle cohesive forces. For soil particles larger than 200 μm, u_{*ts} increases as a result of prevalent dominance of the gravity force. Comparing threshold friction velocities shows that the best agreement between MB and Shao occurs in the saltation size range for $\Gamma = 1.65 \times 10^{-4}$ kg/s^2. *Shao et al.* [2002] and *Tanaka and Chiba* [2005] used $\Gamma = 3 \times 10^{-4}$ kg/s^2, whereas *Zhao et al.* [2006] and *Park et al.* [2007] used $\Gamma = 1.65 \times 10^{-4}$ kg/s^2. The selection of Γ ultimately affects the magnitude of the horizontal and vertical fluxes calculated with the Shao scheme and hence can be used as a tuning parameter. The effect of Γ on the calculated vertical fluxes will be further addressed in section 5.

[16] The threshold friction velocity over a smooth surface depends on the air density and soil particle density (see module 1a in Figures 1 and 2). The majority of the regional dust modeling studies used a constant value for each of these two parameters [e.g., *Uno et al.*, 2001; *Gong et al.*, 2003; *Zhao et al.*, 2006; *Sun et al.*, 2006]. Usually, the air density is selected to be the reference air density at sea level (1.23 kg/m^3), and the density of soil particles is often selected to be the density of quartz (2.65 g/cm^3). *Neuman* [2003] pointed out that changes in temperature, air density, or both may significantly affect the kinematic viscosity and aerodynamic drag force acting on soil particles, thus influencing their entrainment efficiency.

[17] To test the sensitivity of the threshold velocity to changes in air density for the topography of Central and East Asia, we performed a WRF simulation of a dust outbreak that occurred in April 2001. This event is known in the community as the "Perfect Dust Storm" [*Darmenova et al.*, 2005] and is representative of a typical meteorological condition associated with dust storms in this region. Figure 4 shows the time-mean surface air density for the duration of the dust event considered. It is apparent that the spatial pattern of the air density is quite heterogeneous, especially over East Asia because of its complex topography. In this case, the mean air density over the Taklamakan, Gobi, and Central Asian deserts was 1.108, 1.121 and 1.195 kg/m^3, respectively. A relative error of the threshold

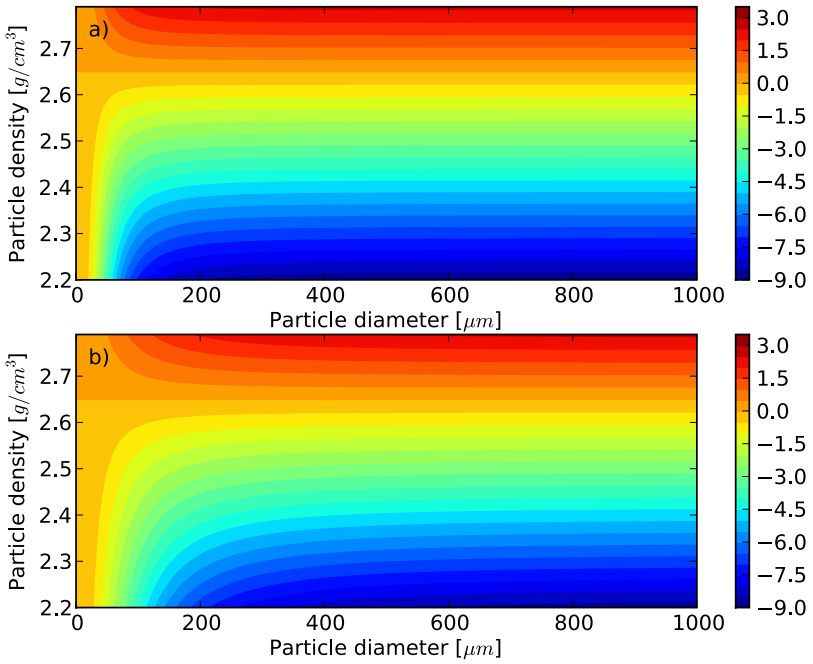

Figure 5. Relative errors (in percent) of the threshold friction velocity over a smooth surface calculated with respect to the quartz density for (a) the MB scheme and (b) the Shao scheme.

friction velocity that will be introduced by using the sea level density instead of actual air density can be calculated as follows:

$$\varepsilon = \frac{u_{*ts}\left(\rho_{ref}\right) - u_{*ts}(\rho')}{u_{*ts}(\rho')}, \qquad (2)$$

where ρ' is the averaged (over the region and time) air density for the Taklamakan, Gobi, or central Asian deserts, and ρ_{ref} is the reference sea level density. Relative errors of u_{*ts} calculated with equation (2) depend only on the ρ_{ref}/ρ' ratio itself and do not vary with the soil particle diameter. Calculated errors were similar for both schemes of about 10%, 11%, and 3% for Gobi, Taklamakan, and Central Asia, respectively.

[18] Furthermore, the threshold velocity over a smooth surface depends on the density of the soil particles, which is ultimately controlled by the mineralogical composition. To investigate this effect, we calculated a relative error of the threshold friction velocity using equation (2), taking a reference density of quartz of 2.65 g/cm^3. The soil particle density was varied between 2.2 and 2.8 g/cm^3 (the values most commonly used in the literature range between 2.5 and 2.75 g/cm^3; see *Petrov* [1976]). Figure 5 shows that the relative error varies with particle diameter, reaching up to 9% for soil particle density of 2.2 g/cm^3.

[19] Although the soil particle density is fixed in the models, the air density is a readily available prognostic variable. Thus we believe that using the time- and space-varying modeled air density has an advantage compared to using a fixed value of the sea level air density. However, the lack of mineralogical composition and density measurements of top-surface soils creates a problem in determining the regional distribution of the soil particle density in Central and East Asia. Until new data becomes available, the models will need to rely on a fixed value of the particle density.

3.2. Drag Partition Correction

[20] Two different approaches to account for nonerodible roughness elements have been proposed. One was developed by *Marticorena and Bergametti* [1995], and it involves a partition scheme by *Arya* [1975] and the logarithmic profile theory by *Priesley* [1959]. This approach was mainly developed from relationships between the roughness length, z_0, and roughness densities obtained from field and laboratory measurements. The drag partition correction in this approach has two intrinsic limitations: (1) it is valid for small wakes (z_0 < 1 cm), and (2) it was developed to parameterize solid obstacles only. This poses a problem in applying this approach to partially vegetated surfaces such as mixed grasslands, shrublands, and agricultural/shrubland mosaics, which are common in Central and East Asia. In the case of such porous canopies, the surface roughness length can exceed 1 cm, and aerodynamic interactions between roughness elements and the wind flow could be quite different compared to that of solid obstacles [*Wolfe and Nickling*, 1996]. To accommodate the higher roughness lengths in the case of vegetated surfaces, *MacKinnon et al.* [2004] modified the original Marticorena and Bergametti roughness correction by using field measurements for desert vegetation types in the central Mojave Desert, USA. In particular, they suggested a value of 12,255 for the parameter X [see *MacKinnon et al.*, 2004, equation (20)]. This parameter is tied to the height of the internal boundary layer between the roughness elements.

[21] The MB drag partition model (either in the MB original or MacKinnon formulations) requires two input parameters: the local roughness length of the intervening surface, z_{0s}, and the roughness length, z_0 (often called the aeolian roughness), which is the length scale that character-

Table 1. Measured Aerodynamic Roughness Length in African, North American, and Chinese Deserts

Surface Type	z_0 (cm)	Location	Reference
	Bare Sandy Surfaces		
Flat desert/interdunes	0.004–0.042	Namibia	*Greeley et al.* [1997]
Sand dunes	0.001–0.01	Tunisia	*Marticorena et al.* [2006]
Bare sand surface	0.075	California	*Lancaster and Baas* [1998]
Playa	0.04	Arizona	*Wolfe and Nickling* [1996]
Playa	0.013–0.018	Nevada	*Greeley et al.* [1997]
Playa	0.06	Tunisia	*Marticorena et al.* [2006]
	Bare Gobi Surfaces		
Gravel/cobble sandy surfaces	0.07–1.06	California	*Greeley et al.* [1997]
Gravel gobi	0.07–0.19	China	*Xian et al.* [2002]
	Gobi Surfaces With Low Sparse Vegetation		
Degraded stony pasture	0.06	Tunisia	*Marticorena et al.* [2006]
Low vegetated stony pasture	0.46	Tunisia	*Marticorena et al.* [2006]
Vegetated stony pasture	1.45	Tunisia	*Marticorena et al.* [2006]
Degraded gypseous pasture	0.24	Tunisia	*Marticorena et al.* [2006]
Highly degraded pasture	0.165	Tunisia	*Marticorena et al.* [2006]
	Sandy Surfaces With Low Sparse Vegetation		
Sand mounds/sand grass	0.2–1.32	California	*Lancaster and Baas* [1998]
	Diverse Desert Surfaces (Bare + Vegetated)		
Variety of desert surfaces	0.005–10.37	California	*MacKinnon et al.* [2004]

izes the loss of wind momentum attributable to roughness elements (see module 1b in Figure 1). Table 1 shows values of z_0 measured in several deserts in Africa, North America, and China for different types of erodible surfaces, including bare sandy, bare gobi, sparsely vegetated gobi, sparsely vegetated sandy surfaces, and mixed desert vegetated surfaces. Measurements of z_0 are rare in the arid regions of Central and East Asia. To our knowledge, the work by *Xian et al.* [2002] is the only study that reported z_0 for gobi surfaces located in the Hexi Corridor in China. One can notice that z_0 varies significantly, by four orders of magnitude. The bare sandy surfaces have z_0 from 0.001 to 0.075 cm, whereas the pebbles/cobbles/stones of gobi deserts have higher z_0, ranging from 0.07 to 1.06 cm. The sandy and gobi surfaces mixed with sparse short vegetation exhibit large variability in measured z_0 (from 0.06 to 1.32 cm). *MacKinnon et al.* [2004] reported even higher values up to 10.37 cm for some desert vegetation types, such as hilaria, creosote bush, tall succulents, and a variety of annuals (weeds/flowers/grasses). Since the original MB drag partitioning scheme was designed for solid obstacles only and the MacKinnon parameterization was extended to accommodate a higher roughness due to desert vegetation, it seems appropriate to apply the MB parameterization for bare (sandy + gobi surfaces) and the MacKinnon formulation for vegetated surfaces. Figure 6 shows the roughness

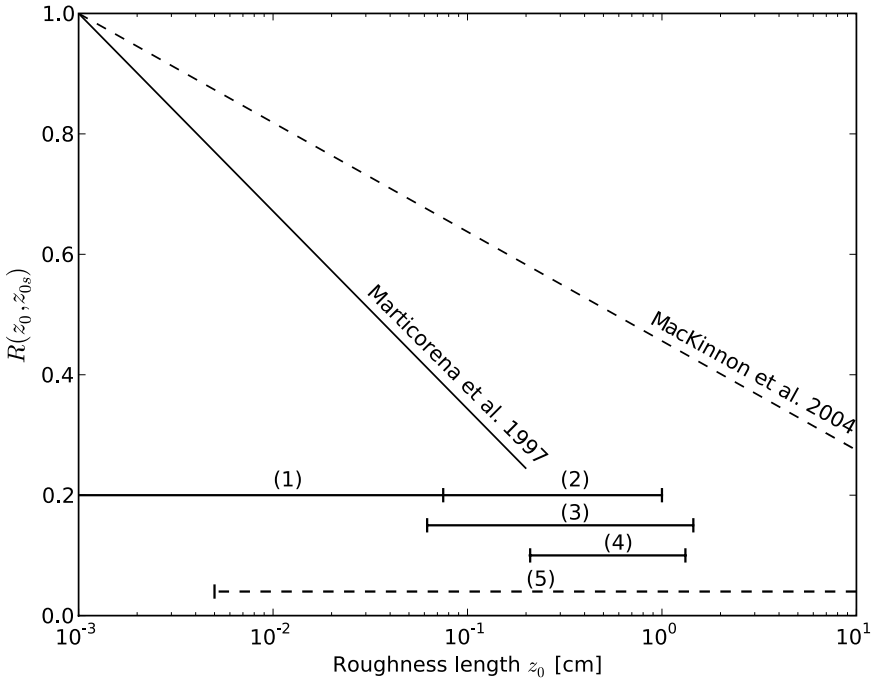

Figure 6. MB drag partition correction calculated with *Marticorena et al.* [1997] and *MacKinnon et al.* [2004] formulations. Horizontal lines show the range of measured roughness lengths for (1) bare sandy surfaces, (2) bare gobi surfaces, (3) sparsely vegetated gobies, (4) sparsely vegetated sandy surfaces, and (5) various desert surfaces.

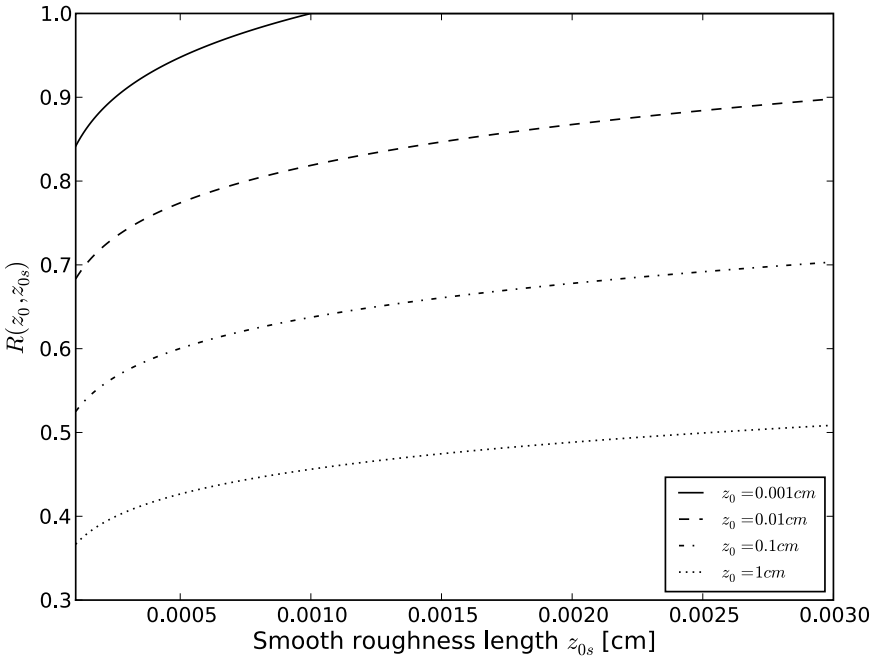

Figure 7. MB drag partition correction as a function of smooth roughness length.

correction $R(z_0, z_{0s})$ calculated with the MB equation (with recent modification of the parameters discussed in the work of *Marticorena et al.* [2006]) and the MacKinnon expression (see module 1b in Figure 1). Figure 6 shows that differences between these parameterizations increase with the increasing aeolian roughness length. The MB roughness correction was calculated only for roughness lengths up to 0.2 cm, since that was the largest value of z_0 considered by *Marticorena et al.* [1997]. Figure 6 also shows the measured values of z_0 for different desert surfaces listed in Table 1. A good separation between bare sandy surfaces and other surface types can be observed. However, z_0 for bare gobi, mixed sparsely vegetated sandy and gobi surfaces, and mixed vegetation surfaces overlap significantly. This reveals a problem in applying the MB or MacKinnon corrections independently for bare and vegetated surfaces. It is apparent that bare gobies, mixed sparsely vegetated gobies, and even densely vegetated surfaces discussed by *MacKinnon et al.* [2004] might have the same roughness. Applying different parameterizations for surfaces with similar roughness values could result in a significant discrepancy in the estimated drag partition. To avoid this discontinuity in $R(z_0, z_{0s})$ and to be able to quantify dust erosion in partially vegetated surfaces such as steppes which are common in Central Asia, we chose to use the *MacKinnon et al.* [2004] parameterization for all surface types. We note that for the most dust-productive, sandy bare surfaces (such as the Taklamakan, sandy deserts in the Alashan Plateau, and most of the Karakum and Kyzylkum) differences with the original MB correction would be the smallest. The effect of the original MB and MacKinnon corrections on vertical fluxes is further examined in section 5.

[22] The MB drag partition also requires a roughness over the smooth surface, z_{0s}. Some studies [*Zender et al.*, 2003; *Gong et al.*, 2003] assumed a constant roughness length of the underlying "smooth" surface, while others [*Marticorena and Bergametti*, 1995; *Laurent et al.*, 2006] calculated the smooth roughness length as 1/30 of the mass median diameter of the coarse mode of undisturbed soil particles. The latter is based on the experimental results of *Greeley and Iversen* [1985], and therefore, the smooth roughness of the underlying surface depends on soil particle size spectra. To examine this issue, we calculated the drag partition correction $R(z_0, z_{0s})$ for a range of z_{0s}, from $z_{0s1} = 1e^{-4}$ cm to $z_{0s2} = 3e^{-3}$ cm. The selected range is based on representative sizes of the fine and coarse modes of the undisturbed soil particle size distributions measured in the deserts of East Asia [*Mei et al.*, 2004]. Figure 7 shows the MB drag partition correction as a function of smooth roughness. $R(z_0, z_{0s})$ is plotted for four different values of z_0: 0.001, 0.01, 0.1 and 1 cm. The u_{*ts}/u_{*t} ratio becomes 1 when $z_{0s} = z_0$. This may be the case in sandy deserts of central and East Asia, i.e., for relatively smooth, bare surfaces. Indeed, *Laurent et al.* [2006] showed that the aeolian roughness retrieved from the POLarization and Directionality of the Earth's Reflectances (POLDER) instrument over the sandy deserts in the Alashan Plateau and the Taklamakan are comparable with the aeolian roughness over the smooth surface.

[23] In turn, the drag partition correction in the Shao scheme is based on an approach suggested by *Raupach et al.* [1993], which is defined in terms of a ratio of the shear stress threshold of the bare erodible surface to the total shear stress threshold of the surface, including the roughness elements. The Raupach *et al.* correction depends on several parameters (see module 1b in Figure 2): β is the ratio of the drag coefficient for a single roughness element to that of the surface without roughness elements; σ is the ratio of the basal to frontal area of the roughness element; m, varying between 0 and 1, accounts for the spatiotemporal variations of the stress of the underlying surface; and λ is the roughness density of the nonerodible elements. Similarly to *Marticorena and Bergametti* [1995], one of the main assumptions of the Raupach drag partitioning is that the roughness is considered as a solid object. However, mea-

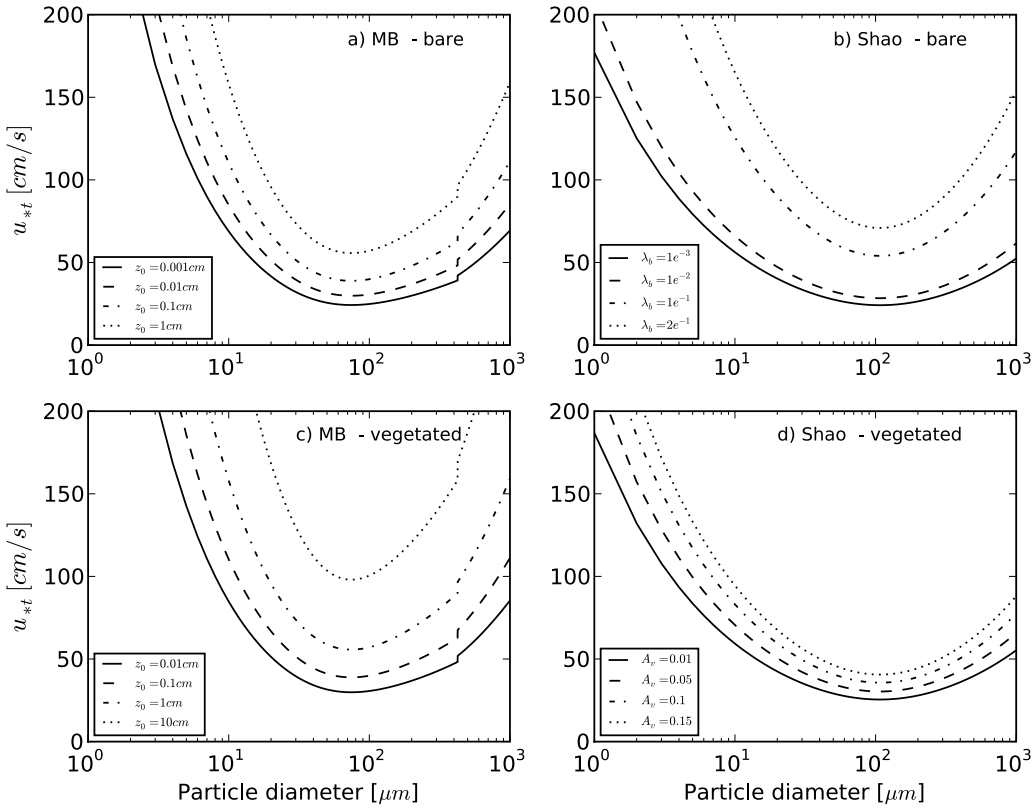

Figure 8. Sensitivity of the MB and Shao threshold friction velocity to drag partition correction parameters for bare and vegetated surfaces.

surements of the drag coefficient for various surfaces covered with different solid and porous obstacles showed that the parameter β, which is partially responsible for representing the drag partition of a single roughness element, varies significantly with the surface type and can be used to describe porous surfaces as well [*King et al.*, 2005]. Reported values of β vary from 72 to 202 depending on the vegetation shape [*King et al.*, 2005]. Thus representative values of β, m, and σ can be selected on the basis of measurements for bare and vegetated surfaces. In turn, the roughness density, λ, is calculated differently for bare and vegetated surfaces. In the case of partially vegetated surfaces, we use the "double drag partition" correction that accounts for both solid obstacles and vegetation (see module 1b in Figure 2). This parameterization requires the roughness densities over the bare (λ_B) and the vegetated (λ_v) surfaces. These parameters vary greatly with the type of the surface and the spatial distribution of roughness elements. To the best of our knowledge, there are no measurements of roughness densities in arid regions of Central and East Asia, but some limited measurements were performed in other regions (e.g., in northern Tunisia; see *Marticorena et al.* [2006]). In the presence of vegetation, we applied the *Shao et al.* [1996] parameterization for λ_v, derived for stubble vegetation with $\lambda_V = -C_\lambda \ln(1 - A_v)$, where A_v is the vegetation cover fraction and C_λ is a coefficient accounting for the distribution and orientation of the roughness elements. Here we adopted the value of $C_\lambda = 0.35$ (following *Shao et al.* [1996]), which is appropriate for stubble roughness. We also considered different values of β, m, and σ for barren and vegetated surfaces, on the basis of available measurements (see module 1b in Figure 2).

[24] Figures 8a and 8b compare the MB (with the MacKinnon version of the drag partitioning correction) and the Shao drag partitioning correction for solid, nonerodible elements. The roughness length, z_0, varies between 1×10^{-3} cm and 1 cm, values that are representative of bare (sandy and gobi) surfaces (Table 1), and λ_B varies between 0.001 and 0.2, on the basis of measurements of *Marticorena et al.* [2006]. It is apparent that for bare surfaces an increase of the roughness (in MB) or roughness density of nonerodible elements, λ_b (in Shao), increases the threshold friction velocity. Both MB and Shao threshold friction velocities are highly sensitive to the presence of vegetation. The MB scheme accounts for vegetation through the increased aeolian roughness, whereas the Shao correction relates vegetation to the vegetation fraction, A_v. Figures 8c and 8d show that an increase in vegetation cover increases the threshold friction velocity in both schemes.

[25] To adequately compare the performance of these two drag partition corrections, it is necessary to establish a relationship between the roughness density and roughness length. An empirical relationship between these parameters was suggested by *Marticorena et al.* [1997] and recently was updated by *Marticorena et al.* [2006]:

$$\begin{aligned} \log(z_0/h) &= 1.31\,\log(\lambda) + 0.66 \quad \lambda < 0.045 \\ \log(z_0/h) &= -1.16 \qquad\qquad\quad \lambda \geq 0.045 \end{aligned}, \tag{3}$$

Table 2. Selected Parameters for Several Types of Bare and Vegetated Desert Surfaces

Number	Case	λ_b	A_v (%)	λ_v	h_b (cm)	h_v (cm)	h_{eff} (cm)	λ_t	z_0 (cm)
			Bare Surface						
1	Sparse solid obstacles	0.002	0	NA	1	NA	1	0.002	0.001
2	Dense solid obstacles	0.15	0	NA	1	NA	1	0.15	0.069
			Vegetated Surface						
3	Sparse short vegetation, sparse solid obstacles	0.002	5	0.018	1	15	13.6	0.02	0.37
4	Sparse short vegetation, dense solid obstacles	0.15	5	0.018	1	15	2.5	0.168	0.17
5	Sparse tall vegetation, sparse solid obstacles	0.002	5	0.018	1	80	72.1	0.02	1.96
6	Sparse tall vegetation, dense solid obstacles	0.15	5	0.018	1	80	9.5	0.168	0.66
7	Dense short vegetation, sparse solid obstacles	0.002	20	0.078	1	15	14.6	0.08	1
8	Dense short vegetation, dense solid obstacles	0.15	20	0.078	1	15	5.8	0.228	0.4
9	Dense tall vegetation, sparse solid obstacles	0.002	20	0.078	1	80	78	0.08	5.38
10	Dense tall vegetation, dense solid obstacles	0.15	20	0.078	1	80	28	0.228	1.93

where h is the geometrical height of the obstacle. Table 2 shows various combinations of vegetation and solid roughness elements constructed to account for the aeolian roughness that occurs in the dust source regions of Central and East Asia. For bare surfaces, we considered two limiting cases: sparse and dense solid elements. For vegetated surfaces, we distinguished between tall and short (sparse or dense) vegetation. The vegetation elements can coexist with solid obstacles such as cobbles, gravel, pebbles or small stones. In each case, we prescribed λ_B, A_v, and the geometrical heights for solid elements (h_b) and for porous elements (h_v), on the basis of representative values for bare and vegetated surfaces for the arid regions. To apply equation (3), the effective heights h_b and h_v of elements should be calculated simultaneously with the total roughness density, λ_t. Then using the empirical relationship (equation (3)), z_0 can be obtained from λ_t.

[26] Figure 9 shows the MB and Shao threshold friction velocities calculated with a consistently introduced pair of λ_t and z_0. The threshold friction velocities show best agreement when solid and porous elements are sparsely located. The largest discrepancy was found in the case of dense vegetation and dense solid elements. In the arid and semiarid regions of Central and East Asia, both regimes may occur. For relatively smooth sandy deserts, the drag partitioning may not be an issue. However, for gobi surfaces, mixed grasslands/shrublands and degraded pastures, roughness densities and roughness lengths may be quite high, hence causing significant biases. According to the USGS land use classification, which is commonly used in models and in WRF, gobi surfaces, grasslands, shrublands and mixed grasslands/shrublands in Central and East Asia cover approximately 1.4 and 5.5 million square kilometers, respectively. For comparison, bare (and sparsely vegetated) surfaces cover only 355,900 km^2 in central Asia and 823,300 km^2 in East Asia.

[27] Along with the choice of a drag partitioning parameterization, an equally important issue is the availability of input parameters at the time and length scales that are characteristic of the aeolian processes. In particular, the MB scheme requires as an input two roughness lengths: smooth roughness length of the bare erodible surface and the roughness length of the overlying obstacles. In turn, the Shao scheme requires vegetation fraction and roughness density for solid elements. Given the high sensitivity to these parameters, an important issue is their availability and their typical range in dust sources in Central and East Asia.

3.2.1. Aeolian Roughness Length

[28] The surface roughness length relevant to the aeolian processes (also known as the aeolian roughness length) is believed to range from centimeters to decimeters [*Marticorena et al.*, 1997]. Past modeling studies used different values of the roughness length for dust sources in East Asia. *Prigent et al.* [2005] and *Laurent et al.* [2006] used the roughness length retrieved from the ERS scatterometer and POLDER data, respectively. *Gong et al.* [2003] and *Zhao et al.* [2006] used the *Marticorena et al.* [1997] relationship between the roughness length, vegetation height and roughness density to calculate the effective roughness length over the model grids. *Liu et al.* [2003] and *Uno et al.* [2001] used a roughness length assigned to the vegetation/land use categories. No past studies considered the aeolian roughness length explicitly in modeling dust emission in Central Asia.

[29] In mesoscale models, the aerodynamic roughness is predefined for different land use categories and is often provided in the form of a look-up table. The problem in using this predefined aerodynamic roughness instead of the aeolian roughness in the dust emission scheme is that they operate on different scales since they are involved in different physical processes. For instance, in WRF the aerodynamic roughness length for bare and sparsely vegetated surfaces is set to 1 cm, whereas *Laurent et al.* [2006] show that for these types of surfaces in East Asia, the POLDER retrieved roughness length varies between 10^{-4} and 10^{-2} cm. How to relate the local aeolian roughness length required in the MB scheme to the scale at which a mesoscale model operates is an important issue and is discussed further in section 4.

3.2.2. Roughness Over Smooth Surfaces

[30] Given the complex geomorphology of Central and East Asian dust sources, use of a constant value for the roughness over a smooth surface would smooth out the heterogeneity of dust sources. We believe that choosing a z_{0s} equal to 1/30 of the coarse mode mass median diameter of the undisturbed soil distribution provides a more realistic representation of dust source textural specifics (fine versus coarse grains).

3.2.3. Vegetation Cover Fraction

[31] A_v is a prognostic variable in many mesoscale models. In WRF it is defined as the grid cell fraction for which midday downward solar insolation is intercepted by a photosynthetically active green canopy [*Chen and Dudhia*, 2001]. The values of A_v are commonly assigned on the

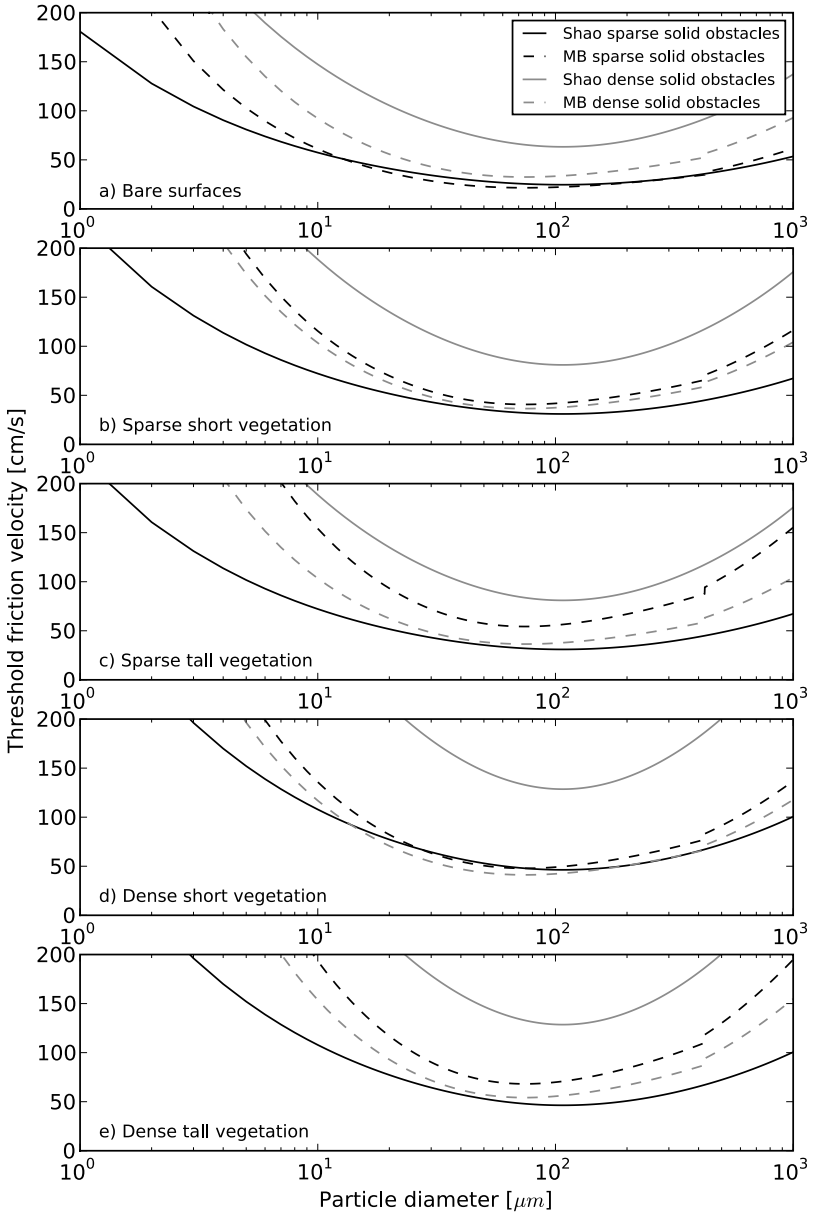

Figure 9. Relationship between the roughness density and roughness length for different surface types in the MB and Shao threshold friction velocity.

basis of the monthly mean data of the green vegetation cover retrieved from satellites [e.g., *Gutman and Ignatov*, 1998]. For instance, in WRF the green vegetation fraction is derived from the NESDIS 0.144-degree monthly 5-year climatology. Then a simple linear interpolation between consequent months is applied to obtain the vegetation fraction for a particular time. Thus if the vegetation fraction from the mesoscale model is used in the dust emission scheme, it would represent some climatologically mean quantity averaged over the model grid cell. Hence, the vegetation fraction would depend on the horizontal model resolution.

3.2.4. Roughness Density of Solid Elements

[32] Although the vegetation cover fraction is readily available in regional models, this is not the case with λ_b. Module 1b in Figure 2 shows that λ_b can be related to the geometrical fractional area, f_c, of the solid elements and their shape factor, η. However, it is difficult to develop a parameterization linking these two parameters because f_c is not available either from measurements or modeling. Since only anecdotal data for λ_b are available, one possibility is to construct a look-up table with representative roughness densities for bare sandy and gobi surfaces (e.g., using measurements of *Marticorena et al.* [2006]) and relate them to particular land use categories in the regional model. One disadvantage of such an approach is that one land use type (e.g., shrublands) may have various types of solid elements and thus assigning one value of λ_b for a particular land use type significantly simplifies the representation of the rough surface.

3.3. Soil Moisture Correction

[33] The MB scheme uses the parameterization developed by *Fecan et al.* [1999], which relates the residual soil

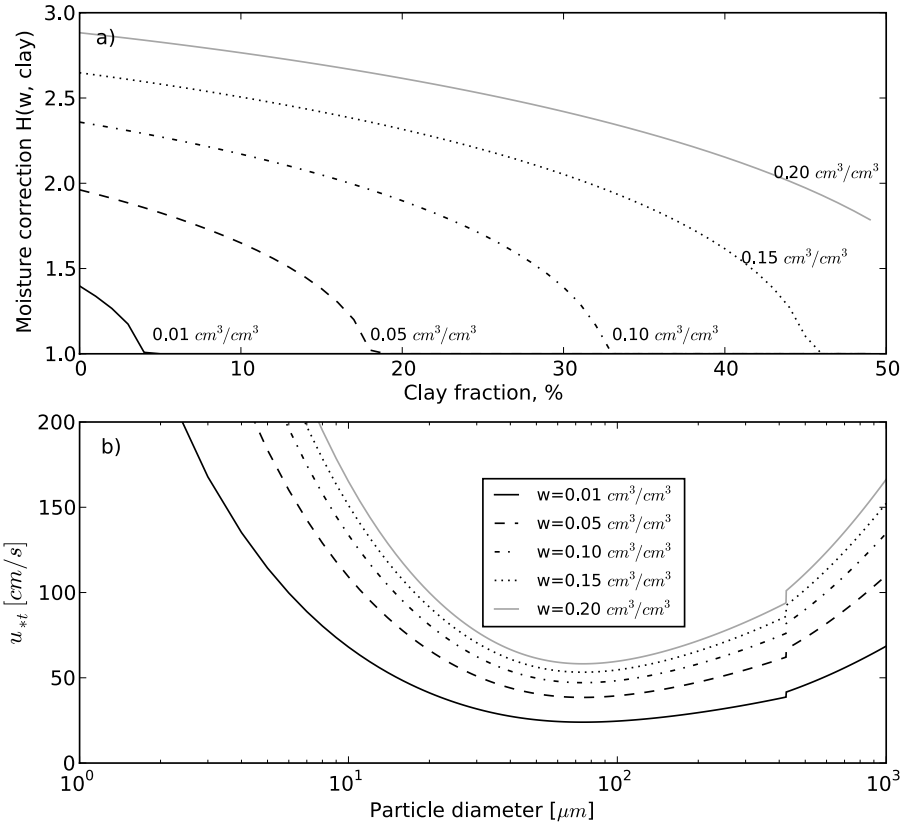

Figure 10. (a) *Fecan et al.* [1999] moisture correction as a function of clay fraction and soil moisture. (b) Sensitivity of the MB threshold friction velocity to the Fecan et al. moisture correction.

moisture to the soil clay content. The parameterization is based on wind tunnel measurements of the increase of the threshold wind velocity (or threshold wind friction velocity) observed for different gravimetric soil moisture (0 to 15%) and 13 soils with texture ranging from pure sand to clay, including sand loam, loamy sand and loamy clay. In turn, the Shao scheme uses an exponential parameterization of soil moisture on the basis of the wind tunnel data for red aeolian soils from *Shao and Raupach* [1992].

[34] The Fecan parameterization requires two input parameters: a gravimetric soil moisture and a clay fraction. Figure 10a shows the Fecan moisture correction $H = u_{*t(wet)}/u_{*t(dry)}$ (see module 1c in Figure 1) as a function of the percentage of clay for several values of the volumetric soil moisture. The volumetric moisture is converted to gravimetric as

$$w_g = w_v \frac{\rho_w}{\rho_b}, \tag{4}$$

where ρ_w and ρ_b are the water and soil bulk densities, respectively. When $H = 1$, the ratio $u_{*t(wet)}/u_{*t(dry)}$ is equal to 1, and the threshold friction velocity is not affected by soil moisture. Figure 10a also shows a decrease in this ratio with the increasing clay percentage. Thus an increase in the percentage of clay results in higher residual moisture w′ (see module 1c in Figure 1) and smaller H. Figure 10b shows the MB threshold friction velocity calculated with the Fecan parameterization for a clay fraction of 3% and soil moisture varying from 0.01 to 0.2 cm^3/cm^3. It is apparent that u_{*t} increases with increasing soil moisture, thereby suppressing mobilization of soil grains.

[35] Figure 11a shows the threshold friction velocity calculated with the soil moisture correction of *Shao et al.* [1996] (module 1c, option 1). Figure 11a shows that u_{*t} becomes unrealistically large for soil moistures above 0.05 cm^3/cm^3. *Zhao et al.* [2006] used a slightly modified version of the *Shao et al.* [1996] parameterization by using different equations for soil moisture larger and smaller than 0.03 cm^3/cm^3 (module 1c, option 2). According to Figure 11b this approach produces even higher threshold friction velocities.

[36] The significant differences between the Fecan and Shao moisture corrections raise the question about the range of variability of soil moisture in Asian dust sources. *Ishizuka et al.* [2005] measured soil moisture in the Taklamakan to be in the range of 0.001–0.015 m^3/m^3 at soil depth of 0–1 cm, indicating that the Shao moisture parameterization can capture well arid conditions in the top 1 cm soil layer. The top 1–2 cm soil layer is the most relevant for dust emission, and both Shao and Fecan parameterizations were designed to operate within this layer. However, measurements of soil moisture in the top 1–2 cm layer are rare. More often soil moisture is measured in the top 0–10 cm layer. *Zhao et al.* [2007] reported values of 0.065 – 0.112 m^3/m^3 in the topmost 10 cm layer in Horqin sandy lands of northeast China. These values are an order of magnitude larger than the 0–1 cm soil moisture measured by Ishizuka *et al.* in the Taklamakan.

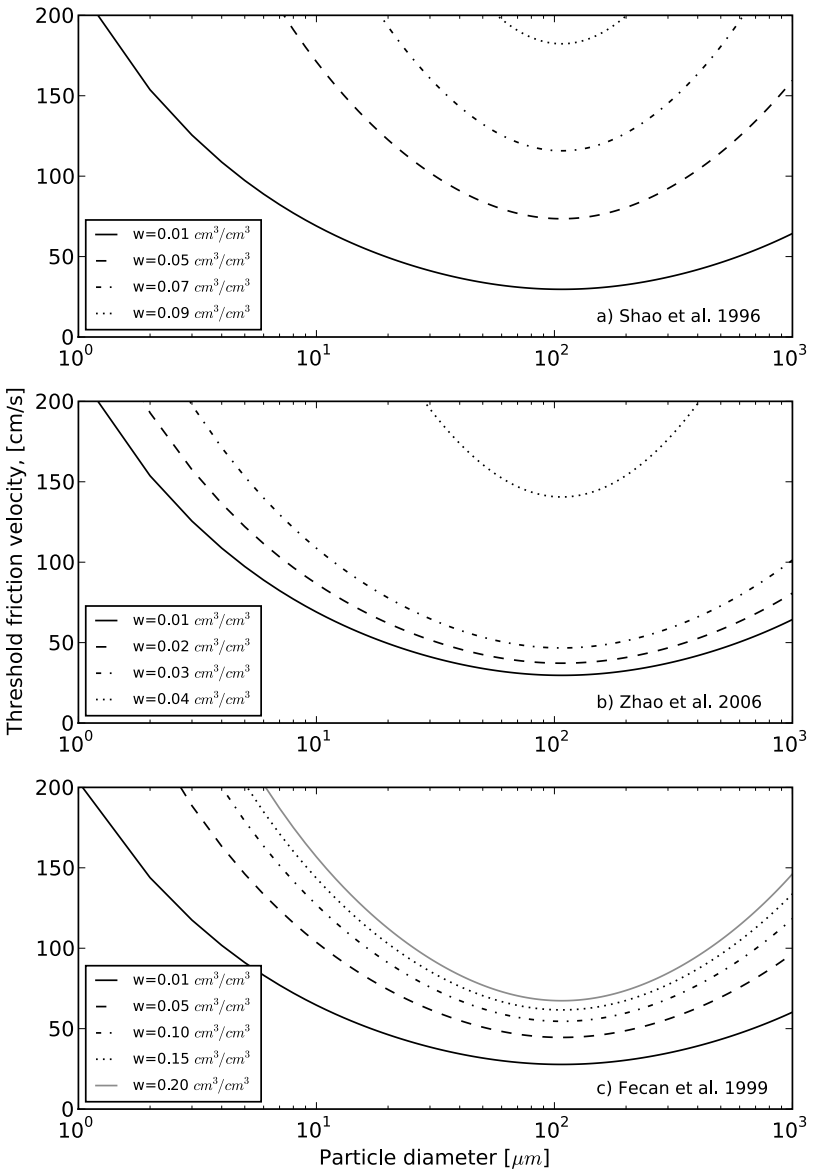

Figure 11. Sensitivity of the Shao threshold friction velocity to soil moisture correction for (a) *Shao et al.* [1996], (b) *Shao et al.* [1996] with modifications of *Zhao et al.* [2006], and (c) *Fecan et al.* [1999].

[37] In modeling of the dust emission within the regional (or global) models, it is common to use the soil moisture simulated by the land surface module [e.g., *Gong et al.*, 2003; *Zender et al.*, 2003; *Sun et al.*, 2006; *Zhao et al.*, 2006]. The land surface parameterizations in many mesoscale models (including WRF) calculate volumetric soil moisture in the 4 to 6 soil layers, and the topmost model layer has an average thickness of 5–10 cm or larger. Therefore, using modeled soil moisture may lead to an overestimation of the moisture correction and hence to higher values of the threshold friction velocity. In particular, it is clear that if the modeled soil moisture in the top 5–10 cm is used, the Raupach and Shao moisture correction would completely suppress the dust emission. In addition, this correction cannot handle the semiarid regions where soil moisture is greater than 0.04 cm^3/cm^3. For these reasons, using the Fecan parameterization in both MB and Shao dust emission schemes is more justified. To support this point, Figure 11c shows the Shao threshold friction velocity calculated with the Fecan parameterization. In this case the behavior of u_{*t} in the Shao dust emission scheme is very similar to that of MB.

[38] A study by *Zhao et al.* [2006] concluded that the major biases between the Shao (although they used the *Shao* [2004] dust emission scheme) and MB dust emission schemes are due to differences in moisture corrections. Although our analysis revealed similar differences, we believe that this is not the problem of the dust emission schemes themselves. In fact, both moisture parameterizations produce similar results for $w < 0.03$ m^3/m^3, which appears to be the typical range in the arid regions for the top 0–1 cm soil layer.

4. Horizontal (Saltation) Flux

[39] The MB scheme uses the *White* [1979] saltation formulation, while the Shao scheme utilizes the *Owen* [1964] transport-limited saltation approach. Both formula-

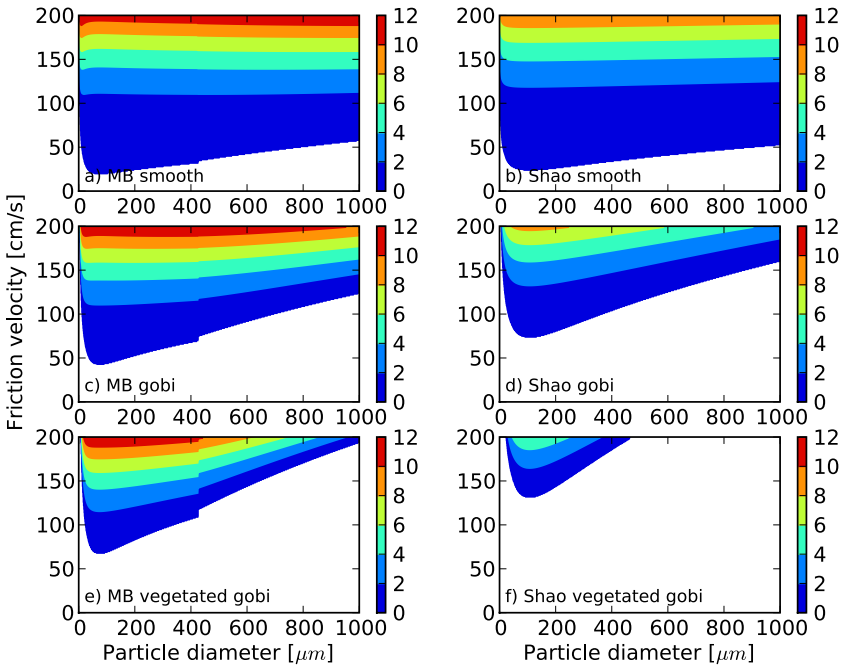

Figure 12. Horizontal (saltation) flux (g/cm^{-1}s^{-1}) as a function of particle diameter and threshold friction velocity for various surface types.

tions depend on the cube of the wind friction velocity and are valid only for uniformly sized soil particles. In the MB and Shao saltation flux equations, c_{MB} and c_{Shao} are dimensionless constants of proportionality (see module 2 in Figures 1 and 2). The original MB scheme [*Marticorena and Bergametti*, 1995] used c_{MB} = 2.61, following the experimental results of *White* [1979]. However, in later modeling studies [*Marticorena et al.*, 1997; *Laurent et al.*, 2006], c_{MB} was set to 1, on the basis of extensive wind tunnel measurements performed for contrasted artificial soil size distributions. In this study, both c_{MB} and c_{Shao} are set to 1.

[40] Figure 12 compares size resolved saltation fluxes as a function of particle diameter and threshold friction velocity calculated with the MB and Shao schemes for the smooth (no roughness elements), bare gobi, and sparsely vegetated gobi surfaces. The roughness correction parameters used in the calculations are listed in Table 2 (cases 2 and 4 for gobi and sparsely vegetated gobi, respectively). The Shao saltation flux is calculated for $\Gamma = 3 \times 10^{-4}$ kg/s^2 (section 3.1). Figure 12 shows that the MB and Shao schemes agree well over a smooth surface, though the MB scheme tends to produce slightly higher saltation fluxes for a given particle size. The only difference between the MB and Shao saltation flux equations for smooth surfaces is in the formulation of the threshold friction velocity and the slightly different equation for the saltation flux. Fluxes were not corrected for moisture or roughness elements. In some sense Figures 12a and 12b show the inherent differences that both schemes start with. As expected, adding roughness elements (gobi and vegetated gobi surfaces) results in a decrease in the saltation fluxes for a particular diameter compared with the smooth surface case (see Figures 12c–12f).

[41] Both the *White* [1979] and *Owen* [1964] saltation models were extended to account for varying soil particles sizes by assuming that the dependence of the saltation flux on u_* and u_{*t} is not affected by the presence of particles with different sizes. Under this assumption the total horizontal flux G is

$$G = \int_{d1}^{d2} Q(D)p(D)\delta D, \tag{5}$$

where d_1 and d_2 define the size range of saltation particles, and $p(D)$ is the soil particle size distribution. In both schemes, G is computed as a weighted integral of the saltation flux Q(D), assuming that the relative contribution of each particle size range to the total horizontal flux is proportional to the relative surface it occupies out of a unit surface (see module 2 in Figures 1 and 2). Despite the slightly different notations used in the total horizontal flux equations in module 2 ($Q_h(D)dS_{rel}(D)$ in MB versus $Q_h(D)p_A(D)\delta D$ in Shao), mathematically both horizontal flux parameterizations are equivalent. Figure 13 shows the total horizontal flux calculated with the MB and Shao formulations for the three types of surfaces as in Figure 12.

[42] To estimate the range of variability in G, we considered two limiting cases of fine and coarse undisturbed soil particle mass size distributions measured by *Mei et al.* [2004] for East Asian deserts. The parameters of the lognormal soil distributions are listed in Table 3. Up to friction velocities of 70 cm/s, fine soils produce higher fluxes compared to coarse soils for smooth surfaces (Figure 13a). Above 70 cm/s, the surface wind-forcing becomes strong enough to mobilize even coarser grains, so

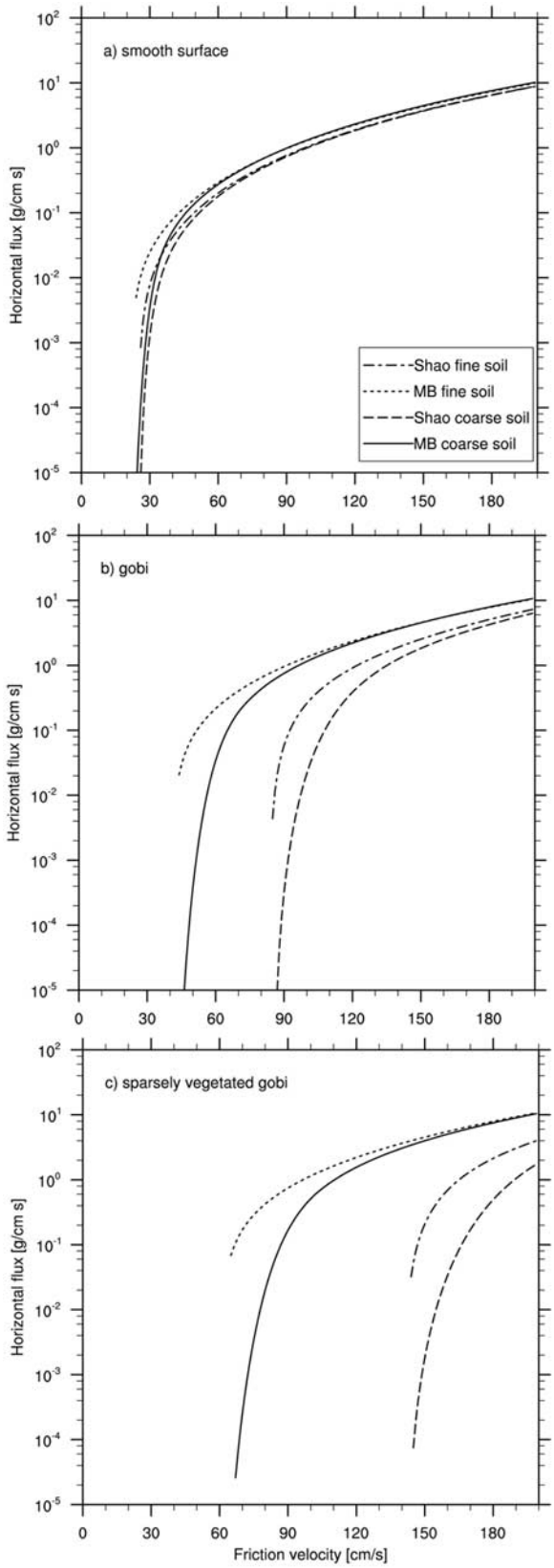

Figure 13. Dependence of the MB and Shao total horizontal flux calculated for coarse and fine soil modes on friction velocity for (a) smooth surface, (b) gobi surface, and (c) sparsely vegetated gobi.

there is practically no difference in the horizontal fluxes originating from fine and coarse soils. The presence of vegetation results in activation of soil particles at higher friction velocities as well as in a decrease in the total horizontal flux for both schemes relative to the smooth surface case (Figures 13b and 13c).

[43] The necessary input parameters for calculating the MB and Shao horizontal fluxes are the soil particle size distribution and the wind friction velocity. Both schemes require undisturbed, dry sieved soil particle size distributions. However, using size distributions derived from the soil texture data is a common approach in the dust modeling studies (section 3.2). The main reason is the very limited data on undisturbed soil particle size distribution available in desert regions [*Mei et al.*, 2004]. With respect to the wind friction velocity, many studies used modeled u_* [*Gong et al.*, 2003; *Zender et al.*, 2003], whereas others [*Marticorena et al.*, 1997; *Laurent et al.*, 2006; *Heinold et al.*, 2007] recalculated u_* either from the modeled 10 m wind velocity U_{10} or from the first model layer wind velocity U_{1st} using the logarithmic layer profile theory. The modeled u_* in the majority of the PBL parameterizations is calculated following the Monin–Obukhov similarity theory:

$$u_* = \frac{kU}{\ln(z_U/z_0) + \Psi_m}, \tag{6}$$

where ψ_m is the stability function accounting for a deviation of the wind profile from the logarithmic, k is the von Karman constant, U is the wind speed at reference height z_U, and z_0 is the aerodynamic roughness length. It is evident that the calculation of u_* depends on the z_0. One significant disadvantage in using the recalculated u_* from the modeled wind speed is the assumption of a neutral PBL and the omission of the stability profile dependence. If U_{10} is used to recalculate u_*, an additional discrepancy comes from the fact that U_{10} in the mesoscale models is commonly calculated from the wind speed at the first model level and u_*, which is calculated using the aerodynamic roughness from the look-up table in the mesoscale model that is different from the aeolian roughness.

[44] The differences in modeled u_* and u_* recalculated from U_{10} assuming the neutral PBL are illustrated in Figures 14a and 14b, which show the time series of u_* during the 2001 dust storm for individual WRF grid cells located in the center of the Taklamakan and Karakum, respectively. There is a very small difference between the WRF-modeled u_* and the u_* recalculated from U_{10} using the default value z_0 in WRF for bare surfaces (i.e., 1 cm). In some sense, the difference between the two curves shows the discrepancies in friction velocity if a neutral

Table 3. Parameters of the Lognormal Soil Particle Mass Distribution

	Mode 1			Mode 2		
Size Distribution	P_1	D_1 (μm)	σ_1	P_2	D_2 (μm)	σ_2
Fine	0.03	442	1.42	0.97	84	1.34
Coarse	1	315	1.29	...	...	...

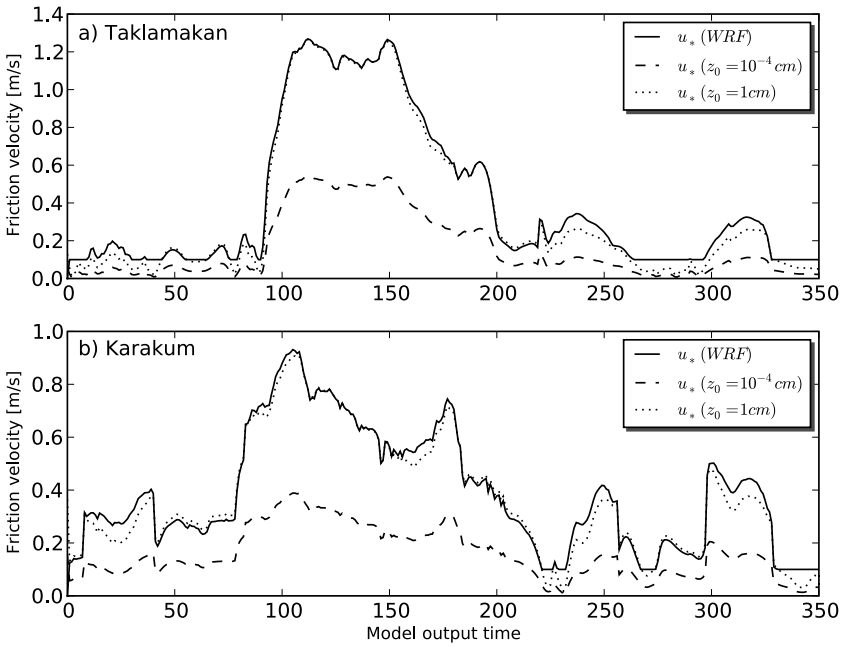

Figure 14. WRF-predicted friction velocity (solid line) and friction velocity recalculated with lognormal wind profile for $z_0 = 1$ cm (dotted line) and for $z_0 = 10^{-4}$ cm (dashed line) for a single grid cell located in (a) the Taklamakan and (b) the Karakum.

PBL is assumed. The discrepancy is smaller for stronger surface winds. This finding implies that during a dust storm, the assumption of a neutral PBL layer might not lead to significant biases in the u_* values. However, if $z_0 = 10^{-4}$ cm is used instead, then differences between the modeled u_* and the recalculated u_* become significant. Thus we can conclude that using an aerodynamic instead of an aeolian roughness will result in larger differences in the friction velocities compared with differences due to adoption of a neutral PBL. There are three possible options in working with the MB dust emission scheme: (1) one can use an external data set of z_0 and recalculate u_* either from modeled U_{10} or reanalysis data, acknowledging discrepancies in saltation fluxes resulting from the assumption of the neutral PBL and/or inaccuracy in U_{10} calculated with the regional model z_0; (2) use an external data set of z_0 and adjust the regional model z_0 to some representative values for bare and sparsely vegetated surfaces in the look-up table, and use modeled u_*; or (3) use the regional model z_0 and u_*, thus keeping the spatial scales consistent, but operating at scales inappropriate for the dust entrainment process. The Shao scheme does not require z_0 to calculate the horizontal fluxes; however, the issue of what u_* to use also concerns this scheme because this affects the magnitude of modeled fluxes.

[45] There are a number of input parameters involved in calculating the horizontal flux. An important question is how to assess the sensitivity of the modeled horizontal flux to different input parameters. Answering this question helps to estimate the relative importance of the input parameters and to facilitate the decision making on the priority of obtaining and improving these parameters within the framework of a regional dust modeling system. To address this issue, we define normalized sensitivity coefficients as follows:

$$s_i = \frac{x_i^c}{G(x_i^c)} \frac{\partial G(x_i)}{\partial x_i}\bigg|_{x_i = x_i^c}, \tag{7}$$

where x_i^c is some representative value of the input parameter x_i, $G(x_i^c)$ is the total horizontal flux calculated at at x_i^c, and $\partial G(x_i)/\partial x_i$ is the partial derivative calculated at x_i^c. Normalized sensitivity coefficients provide a quantitative estimate of the relative change of total horizontal fluxes due to a change in the particular input parameter. For instance, $|s_i| = 10$ means that for a 1% change in the input parameter x_i the total horizontal flux changes by 10%. We calculated absolute values of the sensitivity coefficients for three representative land surface types in central and East Asia: sandy deserts covered with sparse solid obstacles, gobies, and sandy deserts with sparse short vegetation (Figure 15). The representative values of the input parameters for the MB and Shao schemes for each land surface type are listed in Table 4. The sensitivity coefficients were calculated for a range of friction velocities that are called here weak (<40 cm/s), moderate (40–60 cm/s), strong (60–80 cm/s), and severe (>80 cm/s). Figure 15 reveals several important features. First, it is apparent that when wind-forcing increases in sandy deserts, sensitivity of G to land surface parameters decreases. Conversely, for weak and moderate wind speeds in the sandy deserts, horizontal fluxes show higher sensitivity to land surface parameters. The same tendency is also observed for gobi surfaces; however, the distinction between meteorological and surface parameters becomes less pronounced. Despite the fact that fluxes again show high sensitivity to meteorological parameters, the surface

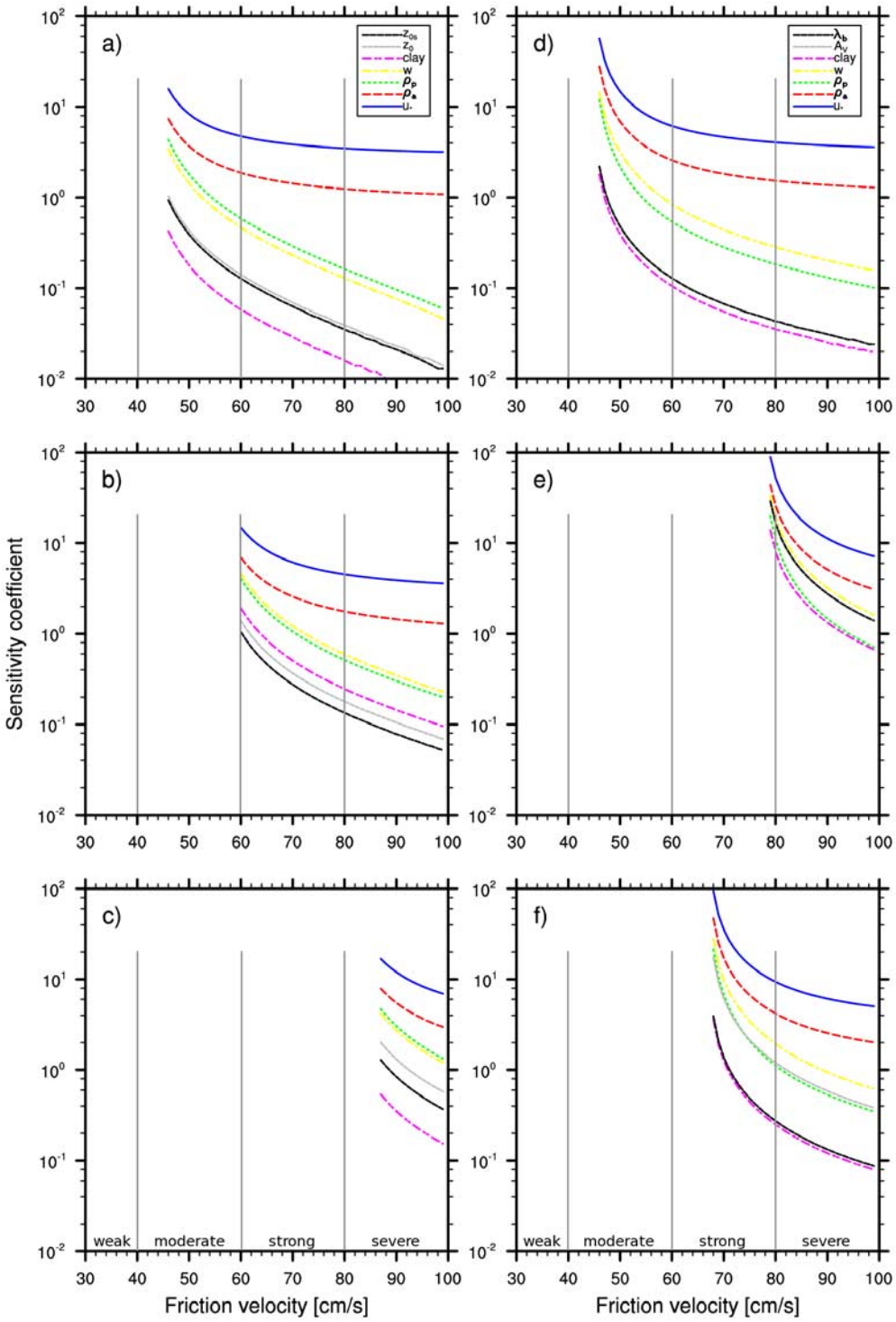

Figure 15. Sensitivity coefficients for horizontal fluxes as a function of wind friction velocity for (a) MB sandy deserts, (b) MB gobi, (c) MB sandy deserts with sparse short vegetation, (d) Shao sandy deserts, (e) Shao gobi, and (f) Shao sandy deserts with sparse short vegetation.

parameters become more important compared to the sandy desert case.

[46] Comparing sensitivity coefficients for the MB and Shao schemes for gobies shows that for the set of parameters listed in Table 4, the MB scheme starts to produce the horizontal fluxes at 60 cm/s, while the Shao scheme gives a nonzero flux at 79 cm/s. For sandy deserts with low sparse vegetation, the Shao scheme starts to lift dust at lower friction velocities compared to the MB scheme. The reason is that in the MB scheme, the magnitude of z_0 controls suppression in u_{*t} from both solid and vegetation elements; thus adding vegetation increases z_0, which then leads to further suppression of the MB horizontal flux. Although the value of λ_b = 0.002 selected for sandy deserts is much smaller than that for

Table 4. Representative Values of the Input Parameters Used in Calculations of Normalized Sensitivity Coefficients

Scheme	Input Parameter (x_i)	Representative Value (x_{ir}) Sandy Desert	Gobi Desert	Sparsely Vegetated Sandy Desert
MB/Shao	u_* (cm/s)	30–100	30–100	30–100
MB/Shao	ρ_a (g/cm^3)	1.121×10^{-3}	1.121×10^{-3}	1.121×10^{-3}
MB/Shao	ρ_p (g/cm^3)	2.65	2.65	2.65
MB/Shao	w (cm^3/cm^3)	0.04	0.06	0.08
MB/Shao	clay fraction (%)	2	9	4
MB	z_0 (cm)	0.001	0.069	0.37
MB	z_{0s} (cm)	1.9×10^{-4}	1.4×10^{-3}	1.4×10^{-3}
Shao	A_v	0.0	0.0	0.05
Shao	λ_B	0.002	0.15	0.002

gobies (0.15) in the Shao scheme, when the vegetation fraction increases (from 0 to 0.05) the decrease in λ_b results in a smaller suppression of u_{*t} compared with the MB scheme. Overall, Figure 15 shows that both schemes respond quite differently to the same surface conditions, which results in differences in the onset and spatial pattern of dust emission between these schemes.

[47] Regardless of the land surface type, both MB and Shao horizontal fluxes are most sensitive to the wind friction velocity, whereas the schemes have different sensitivity for the rest of the parameters depending on the dust source type and representative values selected for the specific land surface type. For instance, we selected relatively low values of soil moistures, vegetation fractions and roughness lengths to reflect typical desert conditions. However, increasing the value of these parameters increases the sensitivity of the horizontal fluxes to these parameters. Nonetheless, it is apparent that wind-forcing is a major factor in dust emission. Surface parameters become increasingly important at moderate to low wind speeds. Therefore, we expect the largest discrepancies between the dust schemes to occur under weak and moderate wind-forcings. An important implication from this finding is that simple dust emission schemes (which have no dependence on land surface parameters) are likely to reproduce well strong and severe dust events, provided that a normalization constant required by simple schemes is determined accurately.

5. Vertical Dust Flux

[48] Module 3b in Figure 1 and module 3a in Figure 2 schematically show calculations of vertical fluxes in the Shao and MB dust emission schemes. The first step in the MB scheme is to compute the horizontal flux for a given soil particle size:

$$dG(D) = Q(D)dS_{rel}(D), \tag{8}$$

where $dS_{rel}(D)$ is the percentage of soil particles, with diameter D relative to the total surface covered by soil particles. Then, the individual kinetic energy of the soil particles with size D is calculated as follows:

$$dF_{kin}(D) = \beta dG(D), \tag{9}$$

where β is an empirically derived parameter equal to 16,300 cm/s^2. For each of the three aerosol size distribution modes (i = 1, 2, 3) given by *Alfaro and Gomes* [2001], the vertical dust particle number flux is computed as follows:

$$dN_i(D) = dF_{kin}(D)p_i(D)/e_i, \tag{10}$$

where e_i and $p_i(D)$ are the binding energy of particles in the ith mode and the fraction of kinetic energy required for the release of dust particle in the ith mode, respectively. The latter is calculated by comparing the individual soil particle kinetic energy:

$$e_c(D) = \rho_p \frac{\pi}{12} D^3 (20u_*)^2, \tag{11}$$

with e_i in the ith mode according to *Alfaro and Gomes* [2001, Table 2]. The last step is to compute the mass emission flux for the ith mode:

$$F_i = \frac{\pi}{6}\rho_p d_i^3 N_i, \tag{12}$$

where N_i is the integral of equation (10) over the soil particle size range and d_i is the mean mass diameter associated to the ith mode [*Alfaro and Gomes*, 2001, Table 1].

[49] In the Shao scheme, the vertical flux of dust aerosol particles of size D_d (commonly referred to as dust-sized particles) caused by bombardment of saltating particles of size D_s (sand-sized particles) is expressed as follows:

$$\tilde{F}(D_d, D_s) = \alpha(D_d, D_s)Q(D_s), \tag{13}$$

where α is the sandblasting mass efficiency in units of [m^{-1}]. Two different formulations of α exist in the literature. The first one was given by *Shao et al.* [1996]:

$$\alpha_{Shao96} = \frac{2}{3}\frac{\rho_p}{\rho_a}\frac{\beta\gamma g}{u_{*t}^2(D_d)}, \tag{14}$$

where γ is a dimensionless constant of 2.5, g is the acceleration of gravity, and ρ_p and ρ_a are particle and air densities, respectively. Here $\beta = \beta(D_d, D_s)$ is a dimensionless empirical function of D_d and D_s derived from the wind-tunnel observations of *Shao et al.* [1996]:

$$\beta(D_d, D_s) = \left[0.125 \times 10^{-4}\ln(D_s) + 0.328 \times 10^{-4}\right] \cdot \exp(-140.7D_d + 0.37), \tag{15}$$

with D_d and D_s in millimeters.

[50] Another formulation of α was given by *Shao and Leslie* [1997]:

$$\alpha_{Shao97} = \frac{[0.6\ln(D_s) + 1.6]\exp(-140D_d)}{u_{*t}^2(D_d)}, \tag{16}$$

with D_d and D_s in millimeters. The dust flux can be computed by performing a double integration:

$$F = \int_{d_1}^{d_2}\int_{0}^{d_1} \tilde{F}(D_d, D_s)p(D_d)p(D_s)\delta D_d \delta D_s, \tag{17}$$

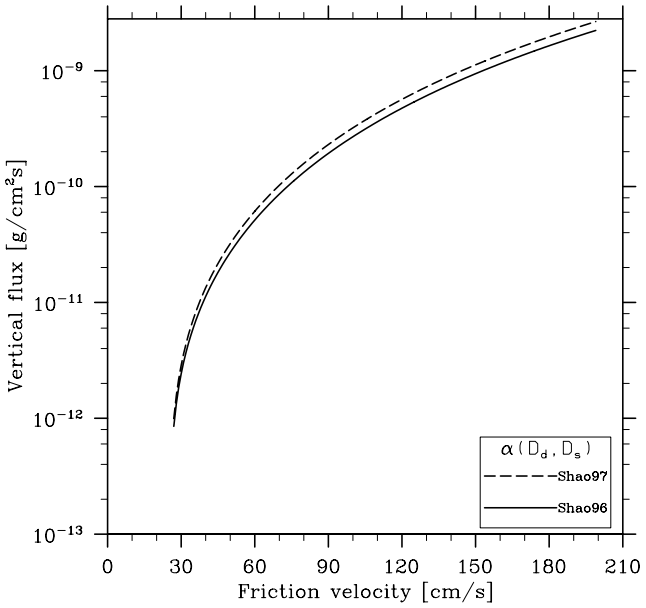

Figure 16. Dependence of Shao vertical fluxes on friction velocity for the *Shao et al.* [1996] and *Shao and Leslie* [1997] formulations of the sandblasting efficiency.

where d_1 and d_2 define the size range ($d_1 < D_s < d_2$) of saltation particles, and $p(D_d)$ and $p(D_s)$ are the mass and surface soil particle size distribution, respectively.

[51] The two formulations describing the sandblasting efficiency are compared in Figure 16, which shows the vertical dust flux calculated with the Shao scheme for selected representative values of input parameters: ρ_p = 2650 kg/m^3, ρ_a = 1.23 kg/m^3, and the acceleration of gravity is g = 9.81 m/s^2. A good agreement between the two curves was observed. Nevertheless, we chose to work with the original *Shao et al.* [1996] formulation for the sandblasting efficiency because it explicitly accounts for the density of air and soil particles. As discussed above, air density affects the threshold friction velocity and saltation fluxes, and thus for the complex topography of Central and East Asia, it would be desirable to account for the effect of varying air density.

[52] As seen from equation (17), the magnitude of the Shao vertical dust flux depends on the distinction of dust and sand-sized particles. *Shao et al.* [1996] defined dust particles as those with fall velocities $w_t(D_d) < 0.5ku_*$, where k is the Von Karman constant and u_* is the wind friction velocity. The fall velocity w_t is given by

$$w_t = \sqrt{\frac{4\left(\rho_p/\rho_a\right)gD}{3C_{DS}(\mathrm{Re}_t)}}, \tag{18}$$

where ρ_p and ρ_a are the particle and air densities, respectively, C_{DS} is the drag coefficient of a sphere, $Re_t = w_tD/\nu$ is the Reynolds number at terminal velocity, and ν is the kinematic air viscosity.

[53] To investigate the range of variability in the dust cutoff particle diameter for representative surface friction velocities calculated by the WRF model during the 2001 Asian dust storm, we calculated D_d via an iterative succession using the following values of C_{DS}:

$$C_{DS} = \begin{cases} 24/\mathrm{Re} & \mathrm{Re} \le 0.1 \\ 22.73/\mathrm{Re} + 0.0903/\mathrm{Re}^2 + 3.69 & 0.1 < \mathrm{Re} \le 1 \\ 29.1667/\mathrm{Re} - 3.8889/\mathrm{Re}^2 + 1.222 & 1 < \mathrm{Re} \le 10 \\ 0.48 & \mathrm{Re} > 10 \end{cases}. \tag{19}$$

[54] Figure 17a shows high surface friction velocities (0.8 – 1.2 m/s) over Mongolian and Chinese Gobi and over the loess plateau on 7 April 2001. In turn, Figure 17b shows that the dust cutoff diameters corresponding to this range of u_* are between 45 and 60 μm. It is evident that the selection of the dust cutoff diameter can significantly influence the Shao vertical dust fluxes. This dependence is illustrated in Figure 18, which presents MB and Shao vertical fluxes as a function of friction velocity for the three land surface types considered in Figure 13. The Shao vertical fluxes were calculated with D_d = 20 μm and D_d = 50 μm. The Shao flux calculated with D_d = 50 μm over a smooth surface (no roughness or moisture correction) shows reasonable agreement with the MB fluxes. Figure 18a shows that practically for the entire friction velocity range, the Shao scheme (with D_d = 50 μm) produces higher vertical fluxes compared with the MB ones. For rougher surfaces (see Figures 18b and 18c), discrepancies in F increase as a result of differences in the threshold friction velocities and different responses of the vertical flux parameterizations to changes in the input parameters.

[55] Figure 19 shows the vertical flux as a function of wind friction velocity calculated with the MB and the MacKinnon corrections for two different z_0 (0.1 and 0.01 cm). Fluxes calculated with the MB roughness correction are more sensitive to changes in z_0 compared with the MacKinnon formulation. Discrepancies in F become more evident for higher roughness lengths. The sensitivity test shows that using the MacKinnon correction produces higher dust loadings compared with the MB formulation.

[56] Figure 20 shows Shao vertical dust fluxes as a function of wind friction velocity for $\Gamma = 1.65 \times 10^{-4}$, 3×10^{-4}, and 5×10^{-4} kg/s^2. The choice of Γ significantly affects the magnitude of dust fluxes and thus Γ can be used as a tuning parameter to control the onset of the particle entrainment and the magnitude of modeled fluxes.

[57] One of the key challenges in developing the dust emission model is the quantification of the binding strength of soil particles [*Shao*, 2000]. It is unlikely that the interparticle cohesion can ever be predicted in theory with the desired accuracy and be implemented in dust emission parameterizations. In addition, there is a large discrepancy in binding energy values between *Alfaro and Gomes* [2001] and *Shao et al.* [1996]. Intrinsic differences in dust emission schemes will affect the modeled dust mass, dust concentration fields in the atmosphere and ultimately the modeled impact of dust on the environment and climate. Overall, we showed that existing differences between the MB and Shao vertical dust fluxes are caused by inherent differences in the

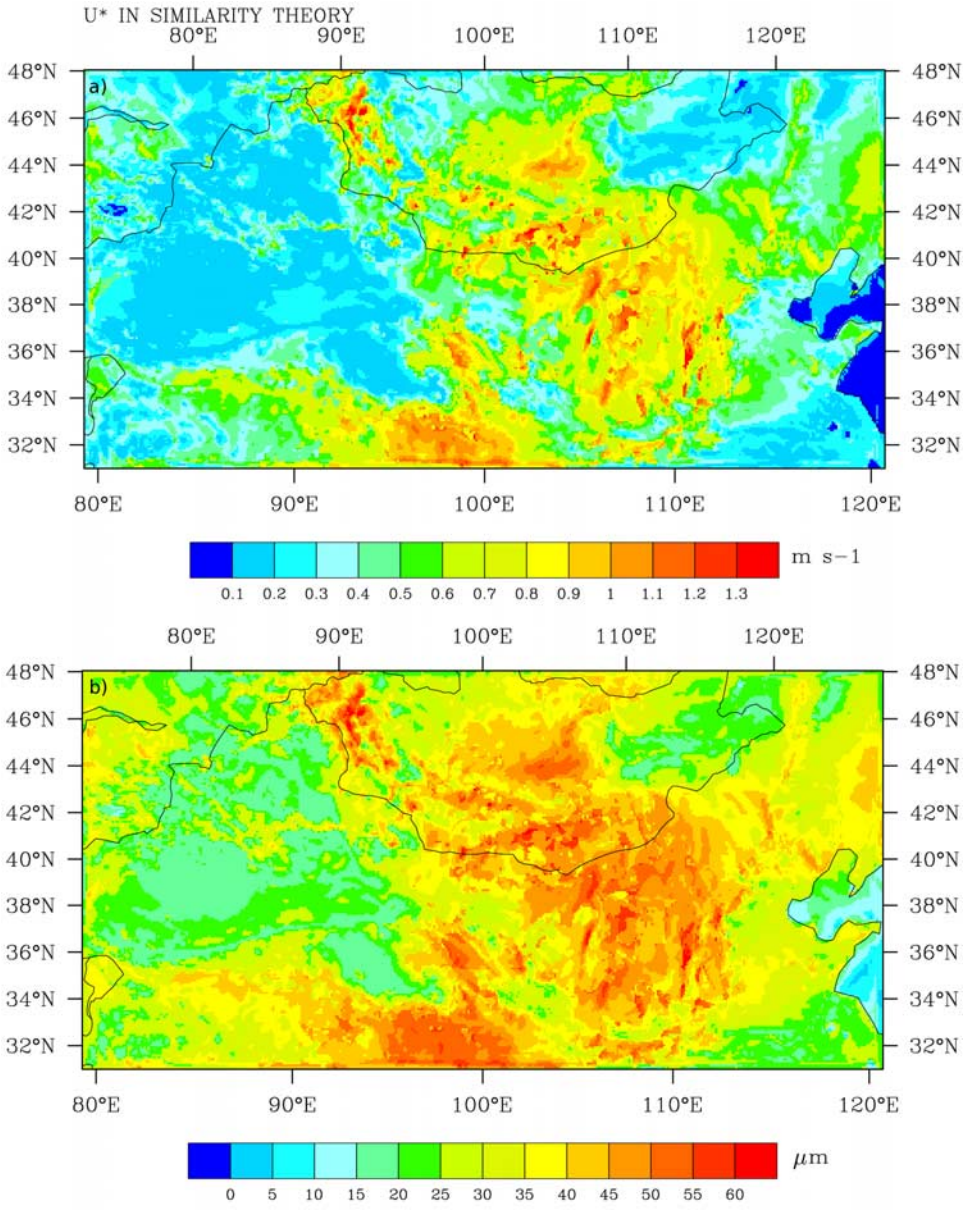

Figure 17. (a) WRF-simulated u_* on 7 April 2001 at 1400 Beijing local time and (b) calculated dust-size particle diameters.

parameterizations of the threshold friction velocities, saltation and vertical fluxes.

6. Case Study of Dust Emission in Central and East Asia

[58] To address the inherent differences in vertical dust fluxes computed with the MB and Shao schemes, we performed simulations of dust emission in Central and East Asia for the month of April 1998. During this time period, there were several strong dust storms in East Asia, with two severe dust outbreaks transported across the Pacific Ocean [*Husar et al.*, 2001]. The spring season of 1998 was also noticeably active in the arid lands of Central Asia.

[59] A new terrestrial preprocessor was developed in support of the WRF-DuMo regional modeling system to represent Asian sources. The preprocessor maps undisturbed soil particle size distributions, POLDER retrieved aeolian roughness lengths, and land use type into a given WRF spatial grid. We used the vegetation fraction, terrain elevation and land use types directly from WRF. The friction velocity was computed from modeled wind speed at 10 m, assuming a neutral stability and using POLDER aeolian roughness length. Soil size distributions for Central and East Asia were taken from a newly developed Undisturbed Soil Particle Size (USPS) distribution database, consisting of dry sieved mass size distributions reported by *Laurent et al.* [2006] and historical measurements in Central Asia. The complete set of the MB and Shao scheme input parameters used in this case study is listed in Table 5.

[60] To account for the surface area that is sheltered by roughness elements within the individual model grid cell,

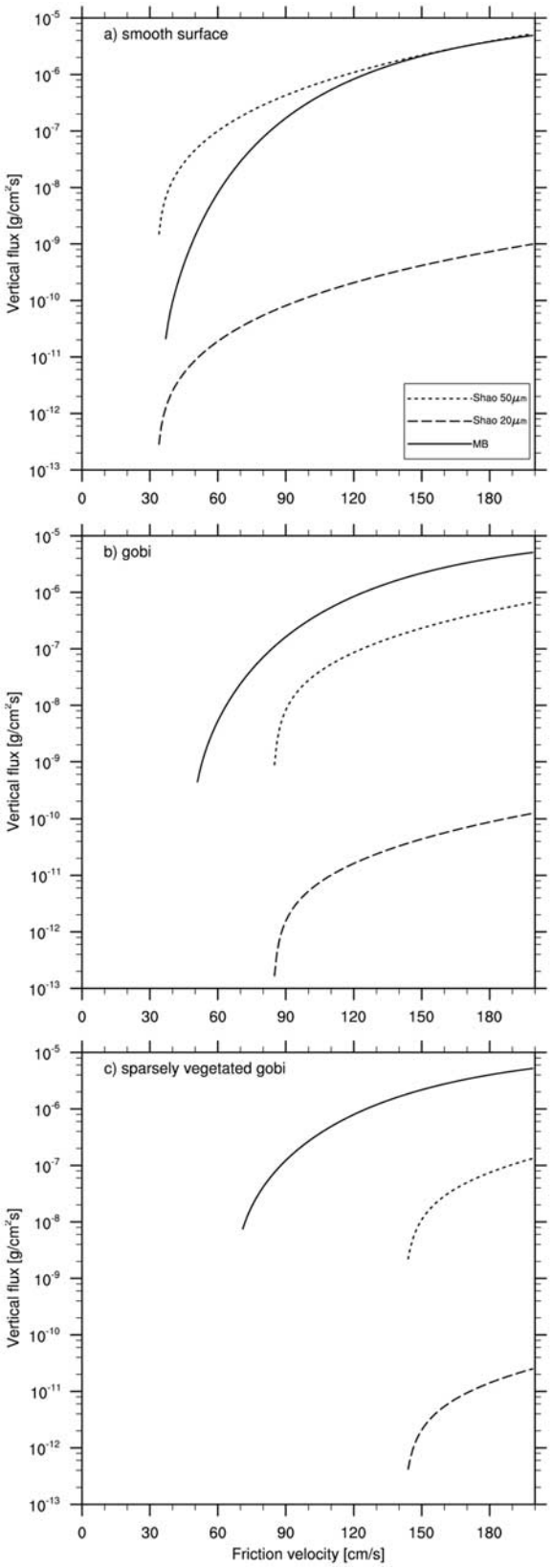

Figure 18. Dependence of MB and Shao vertical dust fluxes on friction velocity for (a) smooth surface, (b) gobi, and (c) sparsely vegetated gobi.

modeled vertical fluxes are commonly multiplied by an erodible fraction [*Laurent et al.*, 2006; *Heinold et al.*, 2007]. In the MB scheme, we followed the *Laurent et al.* [2006] correction to relate erodibility within the grid cell with the roughness length, z_o:

$$E_{MB} = \begin{cases} 1 & \log_{10} z_0 < -2.5 \\ (1 - A_{snow})(-0.085 \log_{10} z_0 + 0.72) & \log_{10} z_0 > -2.5 \end{cases}, \quad (20)$$

where A_{snow} is the WRF-simulated snow cover fraction. In the Shao scheme, we applied the following erodible fraction:

$$E_{Shao} = (1 - A_v)(1 - A_{snow}), \quad (21)$$

where A_v is the WRF-simulated vegetation fraction.

[61] The WRF model offers a variety of advanced physical parameterizations of cloud microphysics, atmospheric radiation, land surface and planetary boundary layer. For this case study, we chose the Noah land module, which has four soil layers in the vertical. We used the NCEP simple ice microphysics scheme, Kain–Fritsch cumulus parameterization scheme, YSU boundary layer scheme, RRTM longwave, and Dudhia's shortwave radiation schemes. The simulations were performed with a single domain configuration in both Asian regions. Model outputs were saved every hour at the 10 km model grid resolution and 37 vertical levels. The WRF was initialized with the NCEP reanalysis data.

[62] Figures 21a and 21b show the monthly average vertical dust fluxes for East Asia calculated using both schemes. Although individual dust storms are sporadic intermittent events, a pattern of monthly mean dust fluxes

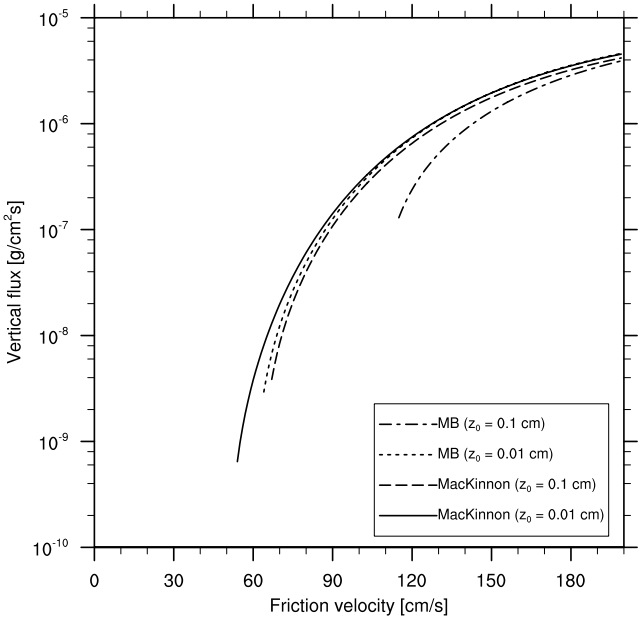

Figure 19. MB vertical fluxes calculated with MB and MacKinnon roughness corrections as a function of friction velocity.

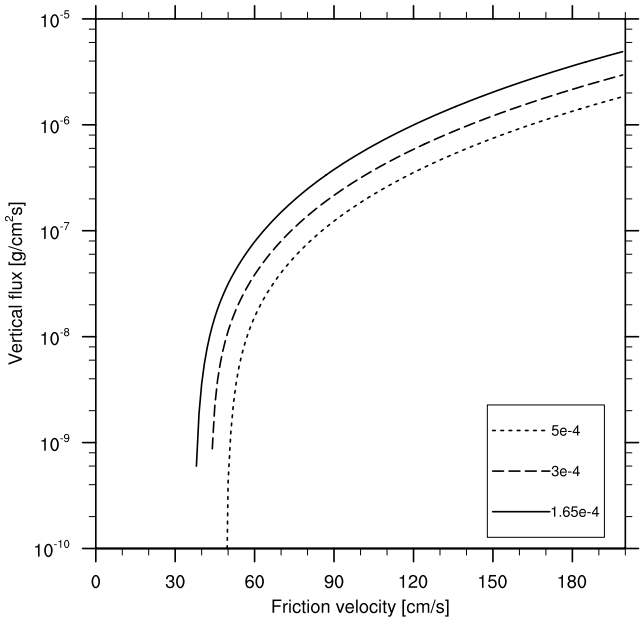

Figure 20. Shao vertical fluxes calculated with three different values of the parameter Γ as a function of friction velocity.

provides useful insights into the dust scheme behavior. It can be seen that the schemes agree well in terms of the spatial distribution of emitted dust across East Asia. Nevertheless, some localized "hot spots" of high dust emission produced by the Shao scheme are apparent over the western Gobi and eastern Taklamakan. In turn, the MB scheme tends to lift dust from larger areas, for instance, from grasslands and shrublands in the Mongolian Gobi. To quantify the difference between the MB and Shao schemes, an absolute error of vertical fluxes was calculated as follows:

$$\delta F = F_{Shao} - F_{MB}, \tag{22}$$

where F_{Shao} and F_{MB} are the monthly average vertical dust fluxes. The absolute errors for the domain of East Asia are shown in Figure 21c. For the majority of grid cells, absolute errors are relatively small, between 1 and 5 g/km^{2}s. The error patterns provide a good illustration of the tendency of emitting dust from preferential sources that differ between the dust schemes.

[63] The negative values of absolute errors indicate sources where the MB scheme overwhelms the Shao scheme. Large positive absolute errors (50 – 150 g/km^{2}s) are observed over the entire Taklamakan and western Gobi region, resulting from the higher fluxes produced by the Shao scheme.

[64] Figures 22a and 22b show the monthly average vertical dust fluxes for Central Asia. Both schemes show the most intense dust emission occurred in the Ustyrt Desert, which is located between the Caspian Sea and the Aral Sea. Unlike the Shao scheme, the MB scheme emits from the semiarid grasslands and sandy-gravel deserts to the north of the Aral Sea and the Balklash Lake. In turn, the Shao scheme produces larger vertical fluxes in the vicinity of the Karabogaz Gol and to the east of the Aral Sea. Figure 22c shows the absolute error patterns for the central Asian domain. Similarly to East Asia, absolute errors are negative in many grid cells, indicating that the MB scheme tends to lift from larger areas compared with Shao. However, large positive absolute errors are observed in the Ustyrt Desert, showing that the Shao scheme predicts much larger dust emission in this dust region compared with the MB scheme.

[65] The tendencies shown in Figures 21 and 22 are valid as long as input parameters used to drive the schemes are similar to those listed in Table 5. If a different set is used, the spatial fields of MB and Shao fluxes might change significantly. For instance, magnitudes and spatiotemporal distributions of vertical fluxes would be changed if the WRF u_* and z_0 are used instead of the lognormally recalculated u_* values and the POLDER z_0. Depending on the source region, some input parameters are more readily available than others, and different parameters may have different quality levels. Therefore, one may expect that biases in the performance of the MB and Shao schemes depend on a dust source region and a specific set of input parameters. Clearly, this poses a challenging problem for model intercomparison. Nevertheless, having two physical dust emission schemes within the same regional model enables one to bracket biases for a given set of input parameters, which would otherwise not be possible with the single dust emission scheme.

7. Summary and Recommendations for Regional Dust Emission Modeling

[66] We analyzed and compared in detail two physically based dust emission schemes that were originally developed by *Marticorena and Bergametti* [1995] and *Shao et al.* [1996], denoted as MB and Shao, respectively. In particular, we examined in depth similarities and differences between physical parameterizations of relevant dust emission pro-

Table 5. Set of Input Parameters for the MB and Shao Schemes

Parameters	MB Scheme	Shao Scheme
Particle density ρ_p	2.65 g cm^{-3}	2.65 g cm^{-3}
Air density ρ_a	WRF simulated	WRF simulated
Roughness length z_0	POLDER retrieved	POLDER retrieved
Smooth roughness length z_{0s}	$MMD_{coarse}/30$	...
Vegetation fraction A_V	...	WRF predicted
Roughness density for solid elements λ_B	...	0.002, bare and sparsely vegetated; 0.031, grasslands, shrublands; 0.051, others
Friction velocity	lognormal formalism (with POLDER z_0)	lognormal formalism (with POLDER z_0)
Soil moisture w	WRF simulated $w \times 0.1$	WRF simulated $w \times 0.1$
Size distribution	undisturbed (dry sieved)	undisturbed (dry sieved)
Snow cover fraction A_{snow}	WRF simulated	WRF simulated
Terrain height	WRF terrain height	WRF terrain height
D_{dust}	...	35 μm
Γ	...	3×10^{-4} kg s^{-2}

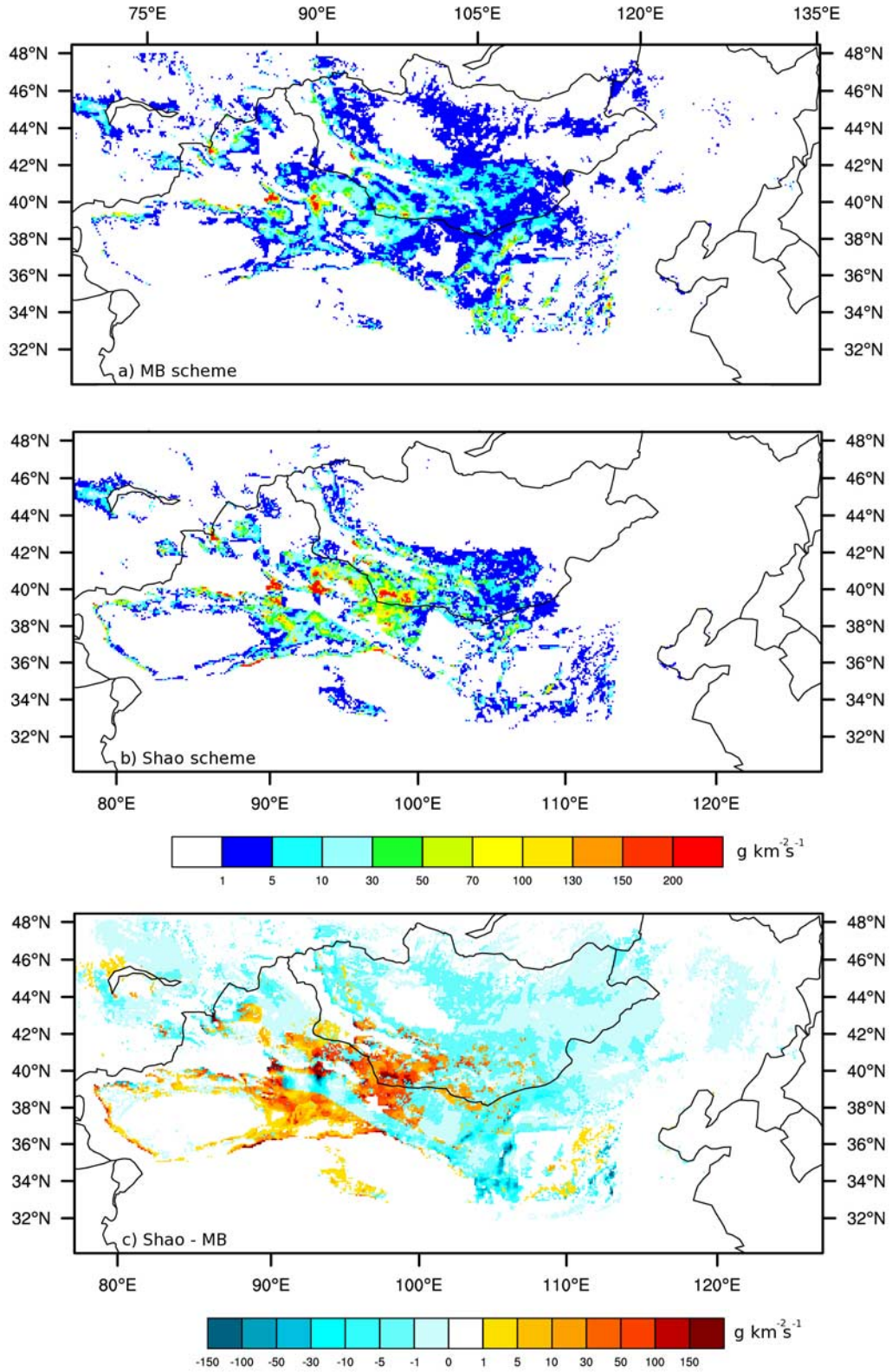

Figure 21. Monthly average vertical dust fluxes for East Asia calculated with (a) the MB scheme, (b) the Shao scheme, and (c) their differences (Shao−MB).

cesses, identified required input parameters, and performed a rigorous sensitivity analysis and intercomparison between these schemes, focusing on the specifics of dust source regions in Central and East Asia.

[67] Our major findings are as follows:

[68] 1. We demonstrated that the main difference between the MB and Shao physical parameterizations of the threshold friction velocity, u_{*ts}, over a smooth surface comes from

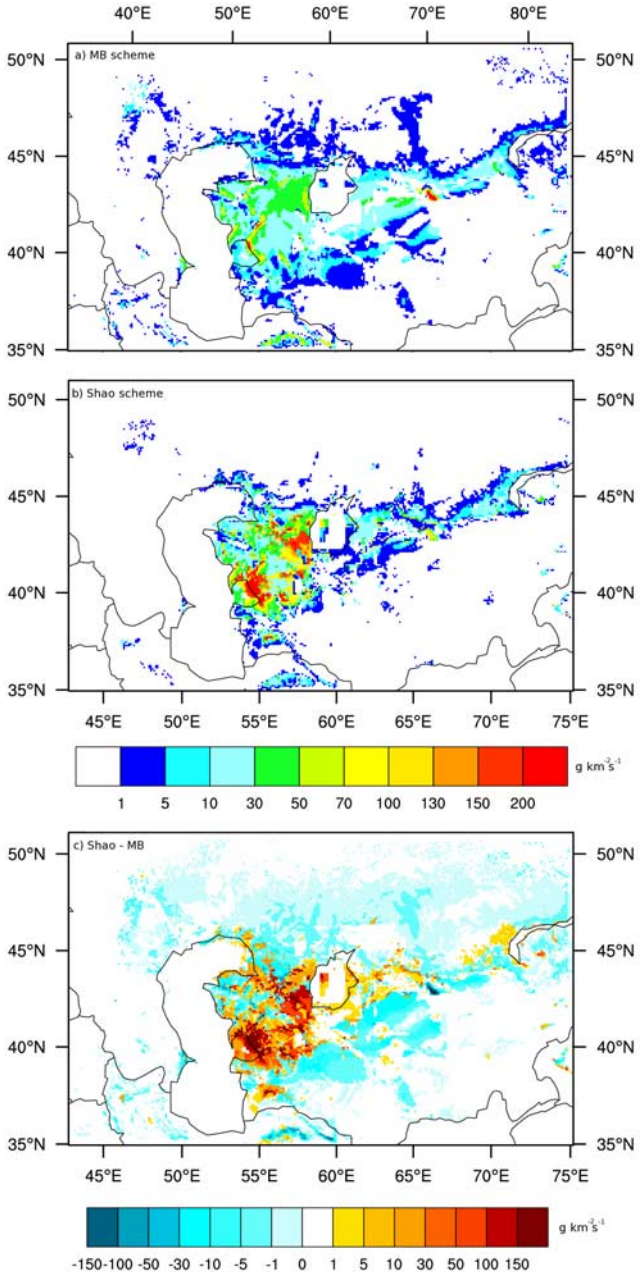

Figure 22. Monthly average vertical dust fluxes for central Asia calculated with (a) the MB scheme, (b) the Shao scheme, and (c) their differences (Shao−MB).

the explicit treatment of cohesive forces in the Shao scheme by assuming that the forces are linearly proportional to soil particle size. Both schemes show similar behavior of the threshold friction velocity as a function of particle diameter. The best agreement between the two parameterizations in the saltation range occurs for $\Gamma = 1.65 \times 10^{-4}$ kg/s^2 in the Shao scheme.

[69] 2. Two different formulations of the MB drag partition were examined: the original [*Marticorena and Bergametti*, 1995] and the modified [*MacKinnon et al.*, 2004]. One advantage of using the MacKinnon formulation is that it accommodates higher roughness lengths that are representative of grasslands and shrublands of central and East Asia. However, the MacKinnon formulation gives a higher dust emission for these land surface types compared to the original MB drag partition scheme. Comparison of MB and Shao drag partition corrections revealed significant differences. To adequately assess the performance of the two drag partition approaches, we used an empirical relationship to link the roughness density with the aeolian roughness. We found that the two drag partition corrections tend to agree better in the case of sparse obstacles, whereas discrepancies in the threshold friction velocities increase in the presence of dense elements.

[70] 3. We found significant discrepancies in the moisture correction between the Fecan et al. and Shao and Raupach approaches for soil moisture greater than 0.03 m^3/m^3. The latter parameterization is derived for hyperarid soils and is not valid for soils with larger moisture content. The Fecan et al. parameterization can accommodate higher moisture, which is better suited to semiarid regions in Central and East Asia.

[71] 4. The MB scheme produces higher size-resolved and total horizontal (saltation) fluxes compared to the Shao scheme. It is demonstrated that the presence of solid roughness elements and vegetation results in activation of soil particles at higher friction velocities, leading to a decrease of total horizontal dust fluxes in both schemes.

[72] 5. Observed discrepancies in vertical dust fluxes between the two schemes are a result of the combined effect of differences in the threshold friction velocity, saltation, and vertical flux parameterizations. The main differences between the *Alfaro and Gomes* [2001] and *Shao et al.* [1996] parameterizations (which are used in the MB and Shao dust emission schemes, respectively) are in the assumed dependence of particle-binding energy on particle size and in the magnitude of the binding energy itself.

[73] 6. We investigated the relative importance of the input parameters required by the MB and Shao dust emission schemes by calculating the normalized sensitivity coefficients of the total horizontal fluxes for surface winds of different intensities. As expected, we found that wind-forcing is one of the most important factors in modeling the dust emission, given that dust emission parameterizations depend on the cube of the wind speed. Dust events occurring under a weak to moderate wind-forcing require special attention, because in this case the surface parameters become of greater importance in governing the efficiency of the dust emission.

[74] 7. The case study simulated with the WRF-DuMo for the month of April 1998 shows good agreement between the MB and Shao schemes in terms of the spatial patterns and magnitudes of monthly emissions in Asian source regions. Most importantly, however, we were able to identify specific differences between the schemes, especially between their performances in individual dust sources. For instance, the Shao scheme tends to emit less from the Hexi Corridor, Badain Jaran Desert, sandy lands in the northeast China, Zaungurskii Karakum, and the semiarid steppe regions to the north of the Aral Sea. But this scheme overwhelms the MB scheme in the Ustyrt Desert, desiccated Aral Sea, and the Taklamakan. The observed tendencies are valid for the input parameters listed in Table 5. We believe that this is an optimal set of parameters for Central and East Asia. It is

difficult to conclude which scheme performs better because of a lack of direct measurements of vertical dust fluxes. However, consistent implementation of the two physical dust emission schemes within the same regional model enables one to bracket biases associated with the modeled dust emission.

[75] Below we provide recommendations on the use of the input parameters required by dust emission schemes within the framework of a regional dust modeling system focusing on Central and East Asia.

[76] Friction velocity and roughness length: We consider these two parameters together since they are intimately connected: roughness length is a necessary parameter in calculating the friction velocity in numerical models. As discussed in section 4, mesoscale model roughness lengths operate at scales unsuitable for dust emission parameterizations. There are three possibilities to handle this issue within a mesoscale model: (1) use an external data set of z_0 and recalculate u_* either from modeled first-layer wind speed, modeled U_{10} or reanalysis data, accepting discrepancies in saltation fluxes as a result of the assumption of the neutral PBL and/or the inaccuracy in U_{10} calculated with the model z_0; (2) use an external data set of z_0 and adjust the model z_0 to some representative values for bare and sparsely vegetated surfaces in the look-up table and use the modeled u_*. This option is only possible if the PBL and land-surface scheme parameterizations in the regional model can operate with aeolian-scale roughness lengths; or (3) use the regional model z_0 and u_*, thus keeping the consistency in the regional, but not the aeolian scales. The Shao scheme does not require z_0; however, the issue of what u_* to use is also important because it affects the magnitude of the modeled fluxes.

[77] Air density: The air density fields exhibit complex spatiotemporal distributions in central and East Asia due to the combined effect of heterogeneous topography and air mass dynamics associated with dust outbreaks. We demonstrated that using the time-varying modeled air density has an advantage compared to using a fixed sea level air density, resulting in more accurate modeling of the dust emission.

[78] Soil particle size distribution, clay fraction, and particle density: Both dust emission schemes require undisturbed particle size distributions. As discussed in section 3.2, past studies have used the soil texture data as a substitution. Using the soil texture instead of undisturbed size distributions results in significant differences in modeled horizontal and vertical dust fluxes. Furthermore, the lack of mineralogical and density measurements creates an obstacle in defining the soil particle density for various soil types in Central and East Asia. As a necessity, a fixed value of the particle density is used in the dust emission schemes regardless of soil type. New data of undisturbed soil particle size distributions and particle density for the uppermost topsoil layer in the Central and East Asia dust production regions would be highly desirable. *Mei et al.* [2004] provide a good example of how to carry out these measurements.

[79] Smooth roughness length: We suggest using a z_{0s} equal to 1/30 of the coarse mode mass median diameter instead of setting it to a fixed constant. This provides more realistic representation of dust source textural specifics (e.g., fine versus coarse soil grains).

[80] Lateral cover for solid roughness elements: Since only anecdotal data for λ_b are available, one possibility is to construct a look-up table with representative roughness densities for bare sandy and gobi surfaces and associate them with land use categories, which are commonly defined in regional models.

[81] Soil moisture and vegetation fraction: Incorporating a dust emission scheme within a regional model enables one to use modeled meteorological and land surface prognostic parameters as an input for the dust scheme. All regional models have a land surface model (LSM) that simulates the soil moisture and vegetation fraction among other variables that are used in modeling the heat, energy, and moisture exchange between the land surface and the atmosphere. These parameters are also required by dust emission schemes. However, a problem is that LSMs currently available in regional models were not designed to model dust emission processes. One important implication is that soil moisture is typically modeled in the top layer about 10 cm thick, while dust emission schemes require the soil moisture content in the top 1–2 cm surface layer. The thicker the layer, the larger the soil moisture content is. Thus an adjustment to modeled soil moisture would be required to avoid the unrealistically high moisture suppression of the dust emission. Alternatively, LSMs can be modified to introduce a thinner (1–2 cm) top layer in addition to 4 to 5 layers that are typically considered in regional modeling. Nevertheless, both the soil moisture and the vegetation fraction will strongly depend on the level of sophistication of LSM itself, as well as a grid size of the regional model. Improvements in LSMs performance at fine scales (~1–10 km) in arid and semiarid regions will ultimately lead to more accurate dust emission modeling within the regional model framework.

[82] Overall, our comprehensive analysis of the MB and Shao dust emission schemes revealed various significant challenges in implementing the physically based treatment of dust emission within a regional model. We identified a number of potential sources that may cause biases in the modeled dust fluxes. First, the physical parameterizations were derived for different conditions, i.e., soil types, roughness elements, etc. Since the equations for the smooth surface threshold velocity, roughness correction, horizontal and vertical fluxes are different, the two schemes will respond differently even to the same input parameters. Second, the schemes involve some common input parameters; however, a few important parameters that are used in the MB scheme are not used by the Shao scheme, and vice versa. Establishing a direct association between these parameters is very difficult, if possible at all. Third, critical data (especially undisturbed soil particle size distributions and aeolian surface roughness) needed to support both schemes are largely missing for Central and East Asia. When data becomes available at the desired spatial resolutions, incorporating it into a regional model will be a straightforward task. Finally, a regional model itself would affect the performance of the dust emission scheme, especially depending on the LSM and PBL parameterizations employed. The very same dust emission scheme incorporated within different regional models may produce quite different dust fluxes in terms of their magnitudes and the

spatial distribution. Thus not only will improving the physical parameterizations of the dust emission be advantageous, but also a new methodological framework for coupling the dust emission scheme with other components of the regional (and global) models that also allows for quantification of errors will be highly desirable.

[83] **Acknowledgments.** This study was supported by the NASA LCLUC program. We thank Anton Darmenov for his help with the development of DuMo and its implementation in WRF. We would also like to thank Benoit Laurent for providing the POLDER roughness data sets.

References

Alfaro, S. C., and L. Gomes (2001), Modeling mineral aerosol production by wind erosion: Emission intensities and aerosol size distributions in source areas, *J. Geophys. Res.*, *106*, 18,075–18,084, doi:10.1029/2000JD900339.

Arya, S. P. S. (1975), Buoyancy effects in a horizontal flat-plate boundary layer, *J. Fluid Mech.*, *68*(2), 321–343, doi:10.1017/S0022112075000833.

Chao, S.-C. (1984), The sandy deserts and the gobi of China, in *Deserts and Arid Lands*, edited by F. El-Baz, pp. 95–115, Springer, New York.

Chen, F., and J. Dudhia (2001), Coupling an advanced land surface hydrology model with the Penn State/NCAR MM5 modeling system. part 1: Model description and implementation, *Mon. Weather Rev.*, *129*, 569–586, doi:10.1175/1520-0493(2001)129<0569:CAALSH>2.0.CO;2.

Darmenova, K., and I. N. Sokolik (2007), Assessing uncertainties in dust emission in the Aral Sea region caused by meteorological fields predicted with a mesoscale model, *Global Planet. Change*, *56*, 297–310, doi:10.1016/j.gloplacha.2006.07.024.

Darmenova, K., I. N. Sokolik, and A. Darmenov (2005), Characterization of east Asian dust outbreaks in the spring of 2001 using ground-based and satellite data, *J. Geophys. Res.*, *110*, D02204, doi:10.1029/2004JD004842.

Duce, R. A. (1995), Sources, distributions, and fluxes of mineral aerosols and their relationship to climate, in *Aerosol Forcing of Climate*, edited by R. J. Charlson and J. Heintzenberg, pp. 43–72, John Wiley, New York.

Fecan, F., B. Marticorena, and G. Bergametti (1999), Parameterization of the increase of the aeolian erosion threshold wind friction velocity due to soil moisture for arid and semi-arid areas, *Ann. Geophys.*, *17*, 149–157, doi:10.1007/s005850050744.

Gong, S. L., X. Y. Zhang, T. L. Zhao, I. G. McKendry, D. A. Jaffe, and N. M. Lu (2003), Characterization of soil dust aerosol in China and its transport and distribution during 2001 ACE-Asia: 2. Model simulation and validation, *J. Geophys. Res.*, *108*(D9), 4262, doi:10.1029/2002JD002633.

Greeley, R. J., and D. Iversen (1985), *Wind as a Geological Process: On Earth, Mars, Venus and Titan*, Cambridge Univ. Press, New York.

Greeley, R. J., et al. (1997), Applications of spaceborne radar laboratory data to the study of aeolian processes, *J. Geophys. Res.*, *102*, 10,971–10,983, doi:10.1029/97JE00518.

Gutman, G., and A. Ignatov (1998), Derivation of green vegetation fraction from NOAA/AVHRR for use in weather prediction models, *Int. J. Remote Sens.*, *19*, 1533–1543, doi:10.1080/014311698215333.

Heinold, B., J. Helmert, O. Hellmuth, R. Wolke, A. Ansmann, B. Marticorena, B. Laurent, and I. Tegen (2007), Regional modeling of Saharan dust events using LM-MUSCAT: Model description and case studies, *J. Geophys. Res.*, *112*, D11204, doi:10.1029/2006JD007443.

Husar, R. B., et al. (2001), Asian dust events of April 1998, *J. Geophys. Res.*, *106*, 18,317–18,330, doi:10.1029/2000JD900788.

Intergovernmental Panel on Climate Change (IPCC) (2007), Summary for policymakers, in *Climate Change 2007: Impacts, Adaptation and Vulnerability. Contribution of Working Group II to the Fourth Assessment Report of the Intergovernmental Panel on Climate Change*, edited by M. L. Parry et al., pp. 7–22, Cambridge Univ. Press, New York.

Ishizuka, M., M. Mikami, Y. Yamada, F. Zeng, and W. Gao (2005), An observational study of soil moisture effects on wind erosion at gobi site in the Taklimakan desert, *J. Geophys. Res.*, *110*, D18S03, doi:10.1029/2004JD004709.

Iversen, J. D., and B. R. White (1982), Saltation threshold on Earth, Mars and Venus, *Sedimentology*, *29*, 111–119, doi:10.1111/j.1365-3091.1982.tb01713.x.

King, J. W., G. Nickling, and J. A. Gillies (2005), Representation of vegetation and other nonerodible elements in Aeolian shear stress partitioning models for predicting transport threshold, *J. Geophys. Res.*, *110*, F04015, doi:10.1029/2004JF000281.

Lancaster, N., and A. Baas (1998), Influence of vegetation cover on sand transport by wind: Field studies at Owens Lake, California, *Earth Surf. Process. Landforms*, *23*, 69–82, doi:10.1002/(SICI)1096-9837(199801)23:1<69::AID-ESP823>3.0.CO;2-G.

Laurent, B., B. Marticorena, G. Bergametti, and F. Mei (2006), Modeling mineral dust emissions from Chinese and Mongolian deserts, *Global Planet. Change*, *52*, 121–141, doi:10.1016/j.gloplacha.2006.02.012.

Lioubimtseva, E., R. Cole, J. M. Adams, and G. Kapustin (2005), Impacts of climate and land-cover changes in arid lands of central Asia, *J. Arid Environ.*, *62*(2), 285–308, doi:10.1016/j.jaridenv.2004.11.005.

Liu, M., D. L. Westphal, S. Wang, A. Shimizu, N. Sugimoto, J. Zhou, and Y. Chen (2003), A high-resolution numerical study of the Asian dust storms of April 2001, *J. Geophys. Res.*, *108*(D23), 8653, doi:10.1029/2002JD003178.

MacKinnon, D. J., G. D. Clow, R. K. Tigges, R. L. Reynolds, and P. S. Chaves Jr. (2004), Comparison of aerodynamically and model-derived roughness lengths (z0) over diverse surfaces, central Mojave Desert, California, USA, *Geomorphology*, *63*, 103–113, doi:10.1016/j.geomorph.2004.03.009.

Marticorena, B., and G. Bergametti (1995), Modeling the atmospheric dust cycle: 1. Design of a soil-derived dust emission scheme, *J. Geophys. Res.*, *100*, 16,415–16,430, doi:10.1029/95JD00690.

Marticorena, B., G. Bergametti, B. Aumont, Y. Callot, C. N'Doumé, and M. Legrand (1997), Modeling the atmospheric dust cycle: 2. Simulation of Saharan dust sources, *J. Geophys. Res.*, *102*, 4387–4404, doi:10.1029/96JD02964.

Marticorena, B., et al. (2006), Surface and aerodynamic roughness in arid and semiarid areas and their relation to radar backscatter coefficient, *J. Geophys. Res.*, *111*, F03017, doi:10.1029/2006JF000462.

Mei, F., Z. Zhang, H. Lu, Z. Shen, and Y. Wang (2004), Characterization of MASDs of surface soils in North China and its influence on estimating dust emission, *Chinese Science Bulletin*, *49*(20), 2169–2175.

Neuman, C. M. (2003), Effects of temperature and humidity upon the entrainment of sedimentary particles by wind, *Boundary Layer Meteorol.*, *108*, 61–89, doi:10.1023/A:1023035201953.

Owen, R. P. (1964), Saltation of uniform grains in air, *J. Fluid Mech.*, *29*, 407–432.

Park, S. H., S. L. Gong, T. L. Zhao, R. J. Vet, V. S. Bouchet, W. Gong, P. A. Makar, M. D. Moran, C. Stroud, and J. Zhang (2007), Simulation of entrainment and transport of dust particles within North America in April 2001 (''Red Dust Episode''), *J. Geophys. Res.*, *112*, D20209, doi:10.1029/2007JD008443.

Petrov, M. P. (1976), *Deserts of the World*, John Wiley, New York.

Priesley, C. H. B. (1959), *Turbulent Transfer in the Lower Atmosphere*, Univ. of Chicago Press, Chicago, Ill.

Prigent, C., I. Tegen, F. Aires, B. Marticorena, and M. Zribi (2005), Estimation of the aerodynamic roughness length in arid and semi-arid regions over the globe with the ERS scatterometer, *J. Geophys. Res.*, *110*, D09205, doi:10.1029/2004JD005370.

Raupach, M. R., D. A. Gillette, and J. F. Leys (1993), The effect of roughness elements on wind erosion threshold, *J. Geophys. Res.*, *98*, 3023–3029, doi:10.1029/92JD01922.

Shao, Y. (2000), *Physics and Modelling of Wind Erosion*, *Atmos. and Oceanogr. Sci. Libr. Ser.*, vol. 23, Springer, New York.

Shao, Y. (2004), Simplification of a dust emission scheme and comparison with data, *J. Geophys. Res.*, *109*, D10202, doi:10.1029/2003JD004372.

Shao, Y., and L. M. Leslie (1997), Wind erosion prediction over the Australian continent, *J. Geophys. Res.*, *102*, 30,091–30,105, doi:10.1029/97JD02298.

Shao, Y., and H. Lu (2000), A simple expression for wind erosion threshold friction velocity, *J. Geophys. Res.*, *105*, 22,437–22,443, doi:10.1029/2000JD900304.

Shao, Y., and M. R. Raupach (1992), The overshoot and equilibration of saltation, *J. Geophys. Res.*, *97*, 20,559–20,564.

Shao, Y., M. R. Raupach, and J. F. Leys (1996), A model for predicting Aeolian sand drift and dust entrainment on scales from paddock to region, *Aust. J. Soil Res.*, *34*, 309–342, doi:10.1071/SR9960309.

Shao, Y., E. Jung, and L. M. Leslie (2002), Numerical prediction of northeast Asian dust storms using an integrated wind erosion modeling system, *J. Geophys. Res.*, *107*(D24), 4814, doi:10.1029/2001JD001493.

Sokolik, I. N. (2003), Dust, in *Encyclopedia of Atmospheric Sciences*, edited by J. Holton, J. Pyle, and J. Curry, pp. 668–672, Academic, London.

Sokolik, I. N., et al. (2001), Introduction to special section: Outstanding problems in quantifying the radiative impacts of mineral dust, *J. Geophys. Res.*, *106*, 18,015–18,027, doi:10.1029/2000JD900498.

Sun, J., L. Zhao, S. Zhao, and R. Zhang (2006), An integrated dust storm prediction system suitable for East Asia and its simulation results, *Global Planet. Change*, *52*(1–4), 71–87, doi:10.1016/j.gloplacha.2006.02.005.

Tanaka, T. Y., and M. Chiba (2005), Global simulation of dust aerosol with a chemical transport model, *J. Meteorol. Sci. Jpn.*, *83*(A), 255–278.

Tegen, I., and I. Fung (1994), Modeling of mineral dust in the atmosphere: Sources, transport, and optical thickness, *J. Geophys. Res.*, *99*, 22,897–22,914, doi:10.1029/94JD01928.

Todd, M. C., et al. (2008), Quantifying uncertainty in estimates of mineral dust flux: An intercomparison of model performance over the Bodélé Depression, northern Chad, *J. Geophys. Res.*, *113*, D24107, doi:10.1029/2008JD010476.

Uno, I., H. Amano, S. Emori, K. Kinoshita, I. Matsui, and N. Sugimoto (2001), Trans-Pacific yellow sand transport observed in April 1998: A numerical simulation, *J. Geophys. Res.*, *106*, 18,331–18,334, doi:10.1029/2000JD900748.

Uno, I., et al. (2006), Dust model intercomparison (DMIP) study over Asia: Overview, *J. Geophys. Res.*, *111*, D12213, doi:10.1029/2005JD006575.

White, B. R. (1979), Soil transport by winds on Mars, *J. Geophys. Res.*, *84*, 4643–4651, doi:10.1029/JB084iB09p04643.

Wolfe, S. A., and W. G. Nickling (1996), Shear stress partitioning in sparsely vegetated desert canopies, *Earth Surf. Process. Landforms*, *21*, 607–619, doi:10.1002/(SICI)1096-9837(199607)21:7<607::AID-ESP660>3.0.CO;2-1.

Xian, X., W. Tao, S. Qingwei, and Z. Weimin (2002), Field and wind-tunnel studies of aerodynamic roughness length, *Boundary Layer Meteorol.*, *104*, 151–163, doi:10.1023/A:1015527725443.

Zender, C. S., H. Bian, and D. Newman (2003), Mineral Dust Entrainment and Deposition (DEAD) model: Description and 1990s dust climatology, *J. Geophys. Res.*, *108*(D14), 4416, doi:10.1029/2002JD002775.

Zhao, H.-L., J.-Y. Cui, R.-L. Zhou, T.-H. Zhang, X.-Y. Zhao, and S. Drake (2007), Soil properties and irrigation effects on five croplands of Inner Mongolia, *Soil Tillage Res.*, *93*, 346–355, doi:10.1016/j.still.2006.05.009.

Zhao, T. L., S. L. Gong, X. Y. Zhang, A. Abdel-Mawgoud, and Y. P. Shao (2006), An assessment of dust emission schemes in modeling east Asian dust storms, *J. Geophys. Res.*, *111*, D05S90, doi:10.1029/2004JD005746.

G. Bergametti and B. Marticorena, Laboratoire Interuniversitaire des Systèmes Atmosphériques, Universités Paris VII-XII, UMR 7583, CNRS, 61 avenue du General de Gaulle, F-9400 Creteil Cedex, France.

K. Darmenova and I. N. Sokolik, School of Earth and Atmospheric Sciences, Georgia Institute of Technology, 311 Ferst Drive, Atlanta, GA 30332, USA. (kdarmenova@eas.gatech.edu)

Y. Shao, Institute of Geophysics and Meteorology, University of Cologne, Kerpenerstrasse 13, Cologne D-50931, Germany.